The Thesis Committee for Siyang Liu
Certifies that this is the approved version of the following thesis:

Synthesis and Systematic Study of Co_3O_4-based Catalysts for Oxygen Reduction and Oxygen Evolution Reactions

APPROVED BY
SUPERVISING COMMITTEE:

Supervisor:

Arumugam Manthiram

Guihua Yu

Synthesis and Systematic Study of Co_3O_4-based Catalysts for Oxygen Reduction and Oxygen Evolution Reactions

by

Siyang Liu, B.E.

Thesis

Presented to the Faculty of the Graduate School of

The University of Texas at Austin

in Partial Fulfillment

of the Requirements

for the Degree of

Master of Science in Engineering

The University of Texas at Austin

May 2015

Acknowledgements

I would like to thank my advisor, Professor Arumugam Manthiram, for allowing me to continue my graduate study in his research group and giving me guidance. I would also like to thank Professor Guihua Yu for being my thesis reader.

I would like to thank Professor Allen J. Bard for helping me understand the basic ideas in electrocatalysis, Dr. L. Li and C. Zu for their generous support during my two years in the group, Dr. H. Ahn for his valuable guidance on electrocatalysis evaluation, Dr. V. Augustyn, N. Colligan, and P. Han for the valuable discussion on OER catalysts, and N. Patterson for helping me conduct some of the experiments. I would also like to thank all the current and previous members in the Manthiram group for their kind and generous help.

Abstract

Synthesis and Systematic Study of Co_3O_4-based Catalysts for Oxygen Reduction and Oxygen Evolution Reactions

Siyang Liu, M.S.E.

The University of Texas at Austin, 2015

Supervisor: Arumugam Manthiram

Co_3O_4-based composite materials are good electrocatalysts for the oxygen reduction reaction (ORR) and the oxygen evolution reaction (OER) in alkaline solutions. Here, this thesis first investigated the individual functionality of Co_3O_4 and the N-doped carbon nanoweb (CNW) in ORR and OER. The Co_3O_4/CNW bifunctional catalysts were synthesized by an *in situ* growth of Co precursors onto CNW followed by a controlled heat treatment. Rotating disk electrode measurements were utilized to provide insight into the specific functions of Co_3O_4 and CNW in the composite material during catalysis. It was found that Co_3O_4 alone exhibited poor ORR catalytic activity. However, in the presence of CNW, Co_3O_4 assisted the selective four-electron oxygen reduction over the two-electron pathway. Co_3O_4 acted as the primary catalytic site for OER and CNW improved the electronic conduction between Co_3O_4 and the current collector. CNW underwent serious degradation at the high potential of the OER, but its stability improved greatly upon the deposition of Co_3O_4. Two possible mechanisms for the improved catalytic stability are discussed. The findings demonstrate the specific functions of Co_3O_4

and CNW in catalyzing the OER and ORR and further establish an understanding of the synergy of the composite in electrocatalysis.

Based on the critical functionality of Co_3O_4 in stabilizing carbon materials in the OER potential region, it is of interest to investigate novel synthesis methods to prepare nano-sized Co_3O_4 that can provide more active sites for catalytic reactions and thus, improve the OER kinetics. Here, *in situ* electrochemical generation of 2-dimensional Co_3O_4 (2D-Co_3O_4) nanoplates were achieved by scanning CoO_x/Co precursors in 1 M KOH solution. X-ray diffraction characterization suggested that CoO_x/Co precursors were oxidized to Co_3O_4 before the onset potential of OER. Scanning electron microscopy showed that oxidation from CoO_x/Co to 2D-Co_3O_4 was associated with the formation of hexagonal nanoplates. The 2D-Co_3O_4 exhibited excellent OER catalytic activity and stability probably due to the effective mass transfer through the 2D structure.

Table of Contents

List of Figures

Chapter 1: Introduction*

1.1 Current Development of Metal-Air Batteries

The increasing demands for energy have stimulated much research interest in renewable energy storage devices. Metal-air batteries consisting of a sandwish strcture of a metal electrode, aqueous or nonaqeous electrolyte, and a catalyst electrode have attracted significant attention due to their higher theoretical energy density compared to the current lithium-ion batteries.[1,2]

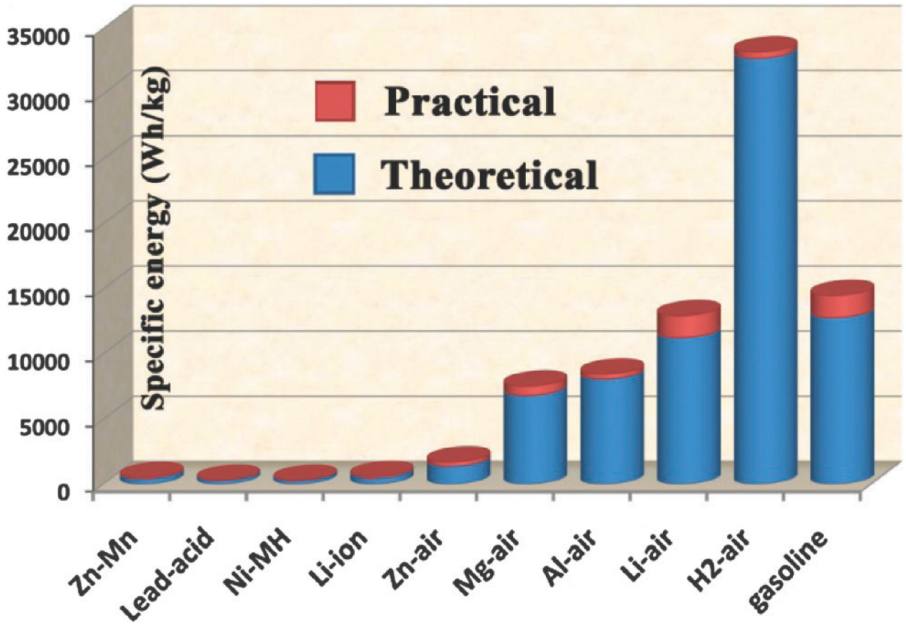

Figure 1.1: Comparison of the specific energy of some primary batteries, rechargeable batteries, metal–air batteries, H_2–air fuel cell, and gasoline.[2]

---

* Liu, S.; Li, L.; Ahn, H. S.; Manthiram, A. "Delineating the Roles of Co3O4 and N-doped Carbon Nanoweb (CNW) in Bifunctional Co_3O_4/CNW Catalysts for Oxygen Reduction and Oxygen Evolution Reactions" *J. Mater. Chem. A.* **2015**, *3*, 11615 – 11623.
S. Liu carried out the experimental work. L. Li and H. S. Ahn provided assistance in electrochemical evaluation analysis. A. Manthiram supervised the project. All participated in the preparation of the manuscript.

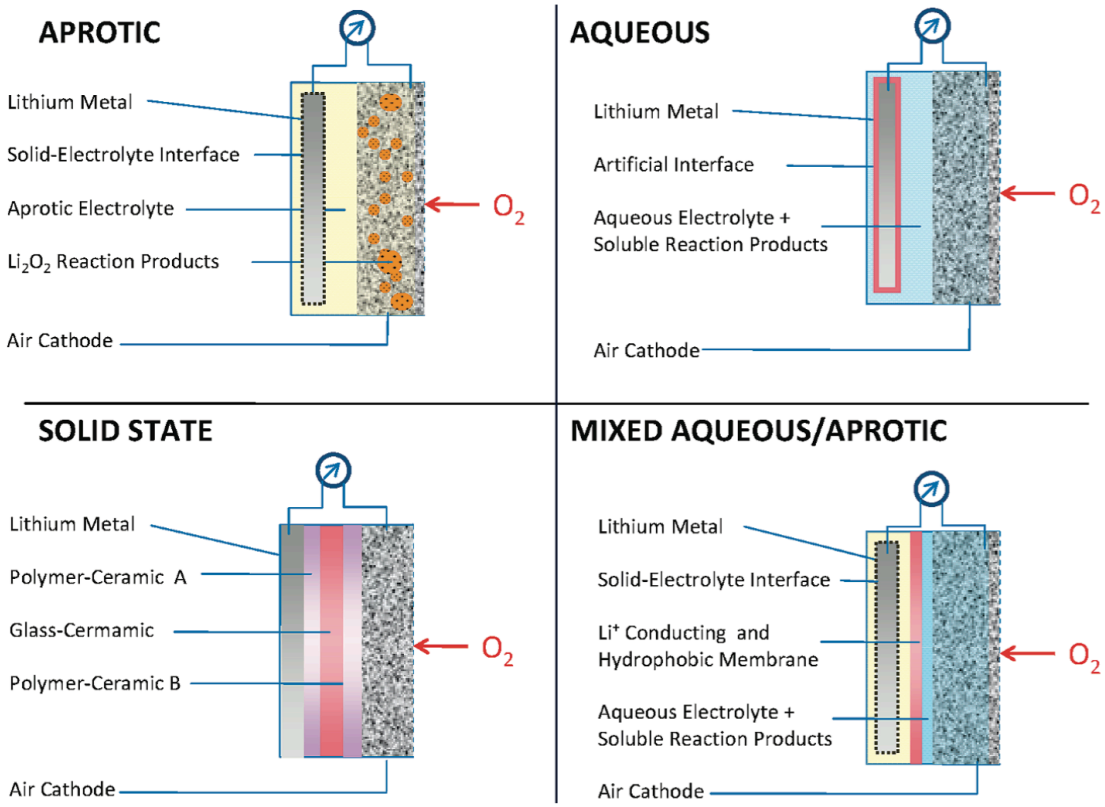

Figure 1.2: Four different configurations of Li-air batteries.[3]

Compared to most metal-air batteries with aprotic electrolytes (dry oxygen operation) and metal-air batteries with acidic electrolytes (expensive metal catalysts that are stable in strong acid operation), metal-air batteries with alkaline electrolytes are promising candidates due to their low operation requirements and abundant catalyst choices.[3-5] However, the sluggish nature of the oxygen reduction reaction (ORR) and oxygen evolution reaction (OER) in alkaline solutions leads to high overpotentials during the discharge and charge process, compromising the round-trip efficiency and impeding the commercialization of alkaline metal-air batteries.[3,6-8] To improve the performance of metal-air batteries, there needs to be a highly efficient catalyst that can catalyze the reduction of O_2 and the oxidation reactions of OH^-. While catalysts such as Pt and IrO_2

exhibit high activity, the high cost and manufacturing difficulties related to the need for well-dispersed particles hinder the commercialization of noble-metal catalysts for metal-air batteries.[5,9-13] Thus, much interest has been drawn towards the development of highly efficient, low-cost catalysts that can facilitate the commercialization of metal-air batteries.

1.2 Discharge Process – Oxygen Reduction Reaction (ORR)

The discharge process of metal-air batteries involves the oxidation of the metal anode, transportation of the electrons through the external circuit to the cathode to break the O=O bonds, and formation of metal hydroxide on the surface of the catalyst.

As has been documented, the oxygen reduction reaction can proceed *via* a direct four-electron pathway,[2]

$$O_2 + 2H_2O + 4e^- \rightarrow 4OH^-;$$

via a two-electron pathway,

$$O_2 + H_2O + 2e^- \rightarrow OH^- + HO_2^-;$$

followed by a further reduction of peroxides,

$$HO_2^- + H_2O + 2e^- \rightarrow 3OH^-;$$

or the decomposition of peroxides:

$$HO_2^- \rightarrow \frac{1}{2}O_2 + OH^-.$$

In order to fulfill the maximum energy utilization, the four-electron pathway is desired. An efficient catalyst is needed to facilitate this process due to the slow kinetics of the ORR. Previous researches have shown that Pt/C favors a four-electron ORR pathway but its use is largely hindered by the cost of platinum.[2,14] To replace Pt, carbon materials have recently attracted much attention due to the low cost and high ORR activity that can be tuned by nitrogen doping.[15-17]

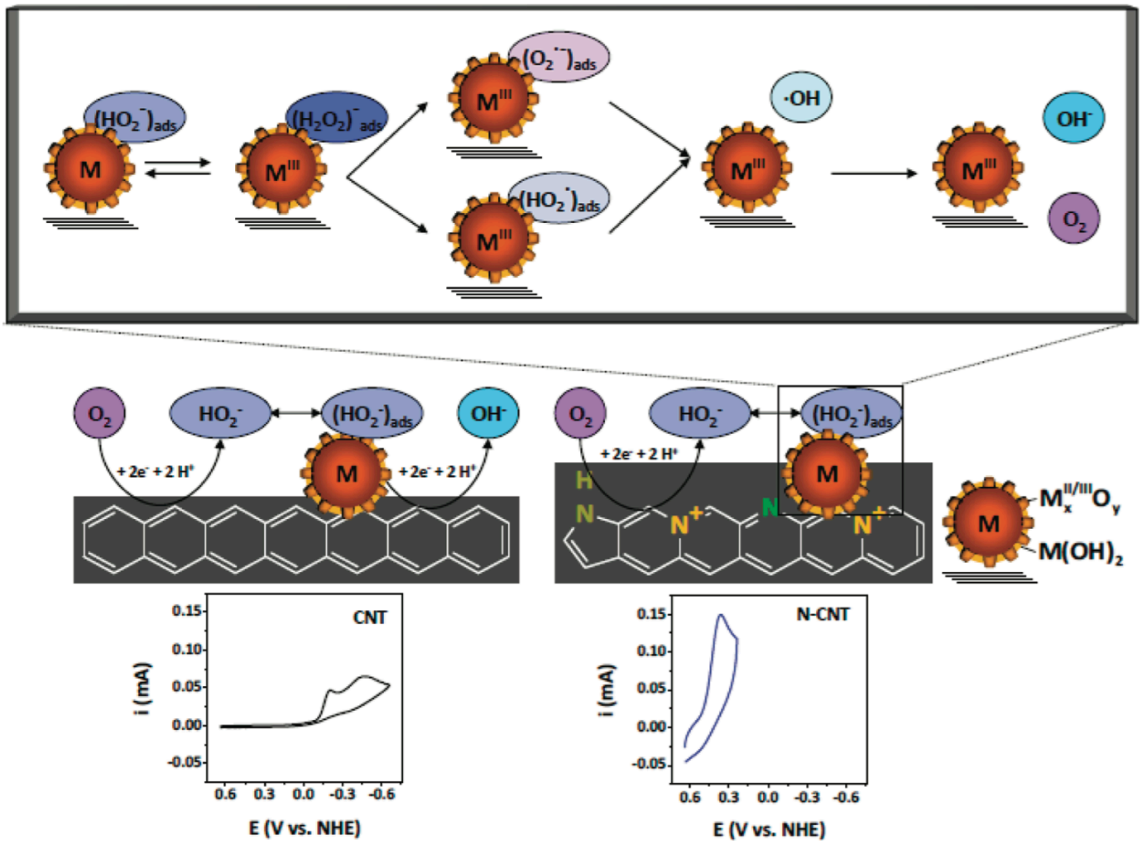

Figure 1.3: ORR mechanism at CNT *vs*. N-CNT electrodes with representative cyclic voltammograms.[18]

It has been reported that with undoped carbon catalysts, ORR is mainly restricted to a two-electron process where peroxides are generated.[18,19] With N-doped carbon materials, the desired four-electron pathway is favored with ORR to produce water. This improvement in catalytic activity has been attributed to the electron-accepting property of nitrogen atoms which leave a positive charge on the nearby carbon atoms to facilitate the breaking of O=O bonds.[15-19] N-doped carbon materials with large surface area and high electronic conductivity such as N-doped carbon nanotubes and N-doped graphene have already been well studied, demonstrating good ORR activities.[10,15-17] Carbon materials with a three-dimensional (3D) network are able to facilitate electron transfer while the

space between the carbon network can improve mass transfer, both of which are beneficial to the ORR kinetics. Therefore, many efforts have been put into studying N-doped carbon materials that possess a 3D geometric structure.[20-22] It ahs been reported N-doped carbon nanoweb (CNW) as a promising 3D carbon catalyst for hybrid Li-air batteries. Its catalytic activity could be further improved by doping with oxygen functional group.[22]

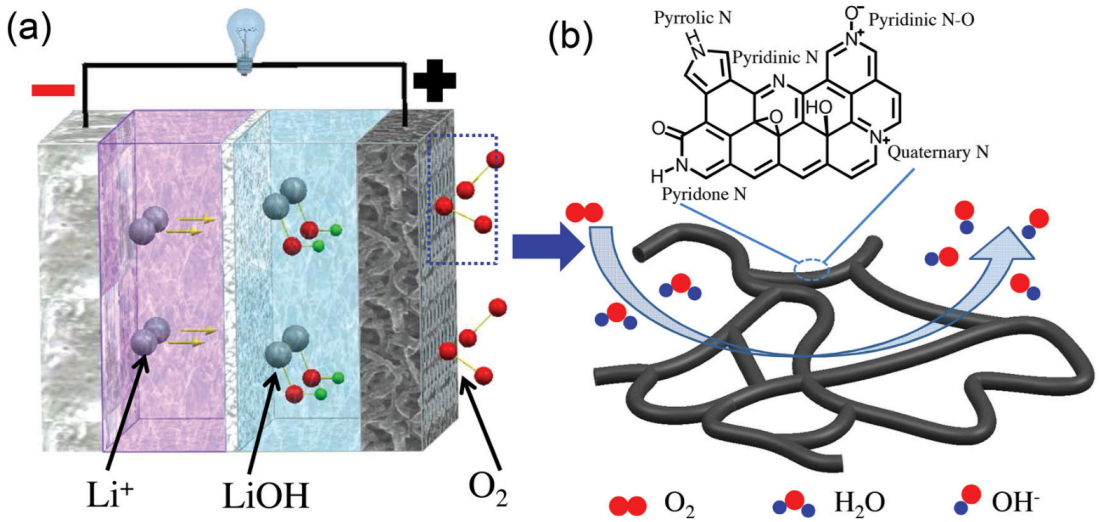

Figure 1.4: (a) Schematic illustration of the aqueous Li-air batteries and (b) ORR on the surface of CNW.[22]

1.3 Charge Process – Oxygen Evolution Reaction (OER)

The charge process of a metal-air battery is the reverse of the discharge where O-H bonds are broken and new O=O bonds are formed:

$$4OH^- \rightarrow 2H_2O + O_2 + 4e^-$$

However, due to the strong binding between O and H, the reaction kinetics of OER are quite sluggish, causing a high onset potential. Thus, the stability of catalysts becomes an important issue to the rechargeability of metal-air batteries.[8] Perovskite oxides have attracted much interest due to their good stability in alkaline solutions than

IrO_2.[23-26] A design principle reported for perovskite oxides points out that the peak OER catalytic activity can be predicted when the number of electrons occupying the e_g orbital of a transition-metal ion is close to one.[23] A previous study has suggested that the surface of perovskite oxide catalysts exhibiting good catalytic activitity undergoes a quick amorphization during OER.[27]

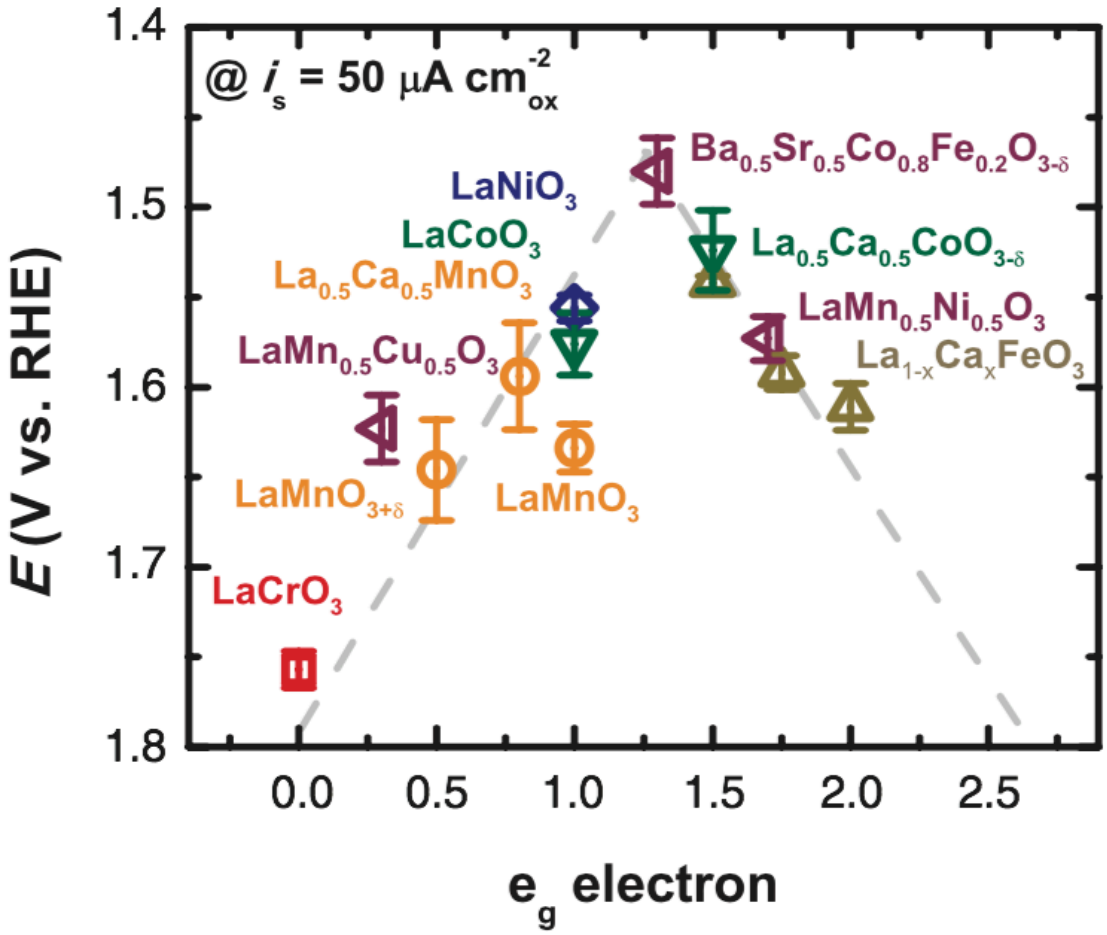

Figure 1.5: The relationship between OER catalytic activities and the e_g occupancy.[23]

Other catalysts, such as Ni-Fe-layered double hydroxides are also appealing candidates for OER.[28-30] Previous investigations into Ni-Fe thin films have demonstrated

that Ni acts as the predominant catalyst for OER. The presence of Fe in the composite system shifts the redox of $Ni(OH)_2$/NiOOH towards a more positive potential, lowering the average oxidation state of Ni.[31] Transition-metal oxides with a spinel structure have also been shown to be promising OER catalysts.[13,32-36] It has been suggested that the abundant defects on the surface of transition-metal oxides improve the catalytic activity by altering the binding between oxygen and metal oxides.[13] Additionally, the direct M-M interactions (M = Co, Mn) across shared octahedral edges of the spinel framework enhance the electronic conductivity of spinel metal oxides, further improving the OER catalytic activity.[37]

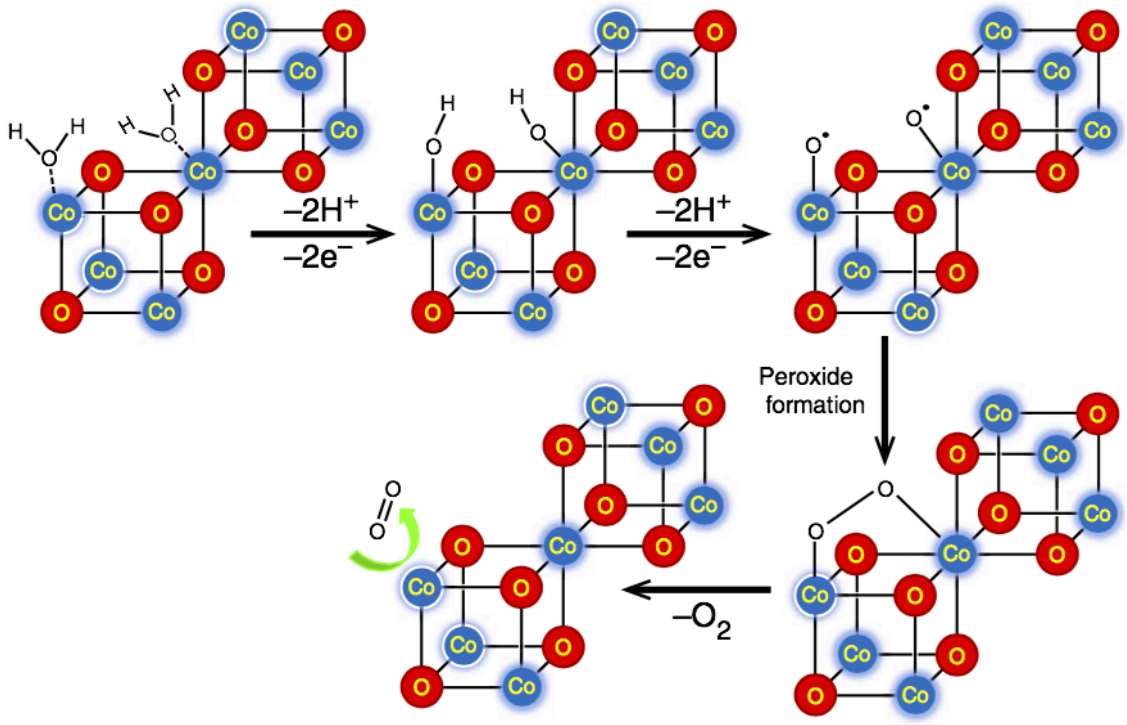

Figure 1.6: OER mechanism on Co_4O_4 cubane units.[37]

Chapter 2: Materials Characterization Techniques

2.1 Scanning Electron Microscopy (SEM)

SEM is a technique where a high-energy electron beam is used to scan the surface of a conductive sample. The resulting signals (secondary electrons) are collected and analyzed to plot an image representing the surface morphology and microstructure of a sample. It can be used in conjunction with the energy dispersive spectroscopy to determine the elementary composition of a sample. SEM characterizations in this thesis were carried out with a Hitachi S-5500 scanning electron microscope at 30 keV.

2.2 Transmission Electron Microscopy (TEM)

TEM is a technique where a high-energy electron beam is used to pass through a thin sample. The atoms of the sample deflect the transmitted electron beam when it passes through the sample. The deflected electron beam is refocused by electromagnetic lenses and forms an image on a screen. This image can be used to study particle size and crystallinity of a sample. TEM characterizations in this thesis were carried out with a JEOL 2010F transmission electron microscope at 200 keV.

2.3 X-ray Diffraction (XRD)

In XRD, the incident X-ray is diffracted by the crystal lattice governed by the Bragg's law of diffraction:

$$n\lambda = 2d\ sin\theta$$

where n is an integer, λ is the wavelength of the X-ray, d is the interplanar spacing of a crystal lattice, and θ is the angle between the incident X-ray and the normal of the crystal plane.

As the diffraction depends on the crystal structure of a material, each material has a specific XRD pattern. Thus, the resulting XRD pattern of a sample can be used to

identify the phase as well as its crystal structure. Powder X-ray diffraction (XRD) data were collected on a Rigaku Ultima IV X-ray diffractometer with filtered Cu K α radiation from 10° to 80°.

2.4 THERMOGRAVIMETRIC ANALYSIS (TGA)

TGA was conducted with a Perkin-Elmer TGA 7 Thermogravimetric Analyzer at a fixed heating rate (5 K min^{-1}) in flowing air from 300 to 1000 K to determine the weight percentage of the Co_3O_4 in the composite materials.

2.5 SURFACE AREA MEASUREMENT

The nitrogen adsorption-desorption isotherms were measured with a gas sorption analyzer (AutoSorb iQ2, Quantachrome Instruments) at 77 K. The Brunner-Emmett-Teller (BET) method with a 7-point BET model was used to calculate the surface area. The correlation coefficient was greater than 0.999.

Chapter 3: Delineating the Roles of Co_3O_4 and N-doped Carbon Nanoweb (CNW) in Bifunctional Co_3O_4/CNW Catalysts for Oxygen Reduction and Oxygen Evolution Reactions*

3.1 INTRODUCTION

Finding bifunctional catalysts with good ORR and OER activities would be highly beneficial to the development of metal-air batteries. Using a single catalyst layer would reduce the total mass of the battery, increasing the overall energy density of the system. Many novel synthetic methods for bifunctional carbon-based metal oxide composites have been reported with an emphasis towards *in situ* growth of Co_3O_4 on carbon materials.[11,12,38-41] The respective roles of the carbon materials and Co_3O_4 in catalyzing the ORR and OER, however, are not clear. In this thesis, the ORR and OER activities of CNW, Co_3O_4, physical mixture of Co_3O_4 and CNW (designated as Co_3O_4 + CNW), and *in situ*-grown composite of Co_3O_4 and CNW (designated as Co_3O_4/CNW) are systematically examed. Based on the experimental data obtained, the contributions of CNW and Co_3O_4 towards ORR and OER are delineated and guidelines for future bifunctional catalyst research are proposed.

3.2 EXPERIMENTAL DETAILS

3.2.1 Chemicals

Cetrimonium bromide ($C_{19}H_{42}BrN$, 99+%, Acros Organics), hydrochloric acid (HCl, 37%, Fisher Scientific), ammonium peroxydisulfate ($(NH_4)_2S_2O_8$, 99.5%, Fisher

---

* Liu, S.; Li, L.; Ahn, H. S.; Manthiram, A. "Delineating the Roles of Co3O4 and N-doped Carbon Nanoweb (CNW) in Bifunctional Co_3O_4/CNW Catalysts for Oxygen Reduction and Oxygen Evolution Reactions" *J. Mater. Chem. A.* **2015**, *3,* 11615 – 11623.
S. Liu carried out the experimental work. L. Li and H. S. Ahn provided assistance in electrochemical evaluation analysis. A. Manthiram supervised the project. All participated in the preparation of the manuscript.

Scientific), pyrrole (C_4H_5N, 99%, Acros Organics), tetracobalt dodecacarbonyl ($Co_4(CO)_{12}$, 98%, Fisher Scientific), hexane (C_6H_{14}, 98.5%, Fisher Scientific), and potassium hydroxide (KOH, 85.3%, Fisher Scientific) were purchased and used as-received.

3.2.2 Synthesis of N-doped Carbon Nanoweb (CNW)

The carbon-nanoweb precursor was synthesized by an oxidative template-assembly method.[22] In a typical synthesis, cetrimonium bromide (CTAB, 7.2 mmol) was dissolved in 1 M HCl (720 mL) in an ice bath. Ammonium peroxydisulfate (21.6 mmol) was dissolved in de-ionized water (120 mL) and then added into the HCl solution. The resulting solution was stirred for 0.5 h before the addition of pyrrole (2.4 mL). The reaction was kept in an ice bath for 4 h under stirring. Then, the black precipitate was vacuum filtered, washed with 1 M HCl and de-ionized water, and dried at 323 K over night. The as-prepared powder was then annealed in a N_2 atmosphere at 1173 K for 3 h.

3.2.3 Synthesis of Co_3O_4/CNW

The Co_3O_4/CNW was synthesized employing a metal carbonyl as the precursor.[42,43] In a typical synthesis, 200 mg of CNW was dispersed in 400 mL of hexane by sonicating for 1 h. Varying amounts of $Co_4(CO)_{12}$ (73.4, 166, and 1000 mmol) were added into the above solution to prepare, respectively, Co_3O_4/CNW-A, Co_3O_4/CNW-B and Co_3O_4/CNW-C. Each mixture was sonicated for another 3 h. The black precipitate was then vacuum filtered, washed with de-ionized water, and dried at 323 K overnight. The controlled heat treatment was carried out in an oven which was preheated to 473 K for at least 1 h in order to obtain a homogeneous temperature. The as-prepared powder

was then treated in the oven for 2 h to obtain Co_3O_4/CNW. Pure $Co_3O_4$was prepared by heating Co_3O_4/CNW-C in a furnace at 623 K for 5 h in air. The physical mixture of Co_3O_4 and CNW was prepared by mixing Co_3O_4 (40 wt.%) with CNW (60 wt.%) and is denoted as Co_3O_4 + CNW.

3.2.4 Electrocatalyst Characterization

All electrochemical tests were conducted in KOH solutions at room temperature. The pH values were measured with a 313P pH Meter (Pinnacle) for KOH concentrations of 0.05, 0.1, 0.2, 0.5, 0.8 and 1 M and were found to be, respectively, 12.65, 12.81, 13.17, 13.49, 13.66, 13.84. A saturated calomel electrode (SCE) was used as the reference electrode. A platinum mesh was used as the counter electrode. The equilibrium potential for oxygen evolution at a given pH is (1.23 - 0.244 – (0.059 × pH)) V *vs*. SCE.

The catalytic performance of CNW, Co_3O_4, the physical mixture of Co_3O_4 and CNW, and Co_3O_4/CNW was tested in a standard rotating disk electrode (RDE) setup with an Autolab PGSTAT302N potentiostat (Eco Chemie B.V.). The catalyst ink was prepared by sonicating a mixture of active material (5 mg), a 2:1 (v/v) solution of Nafion (LQ-1105; Ion Power, Inc.) and 0.1 M NaOH (61.6 μL), deionized water (0.8 mL), and isopropanol (0.2 mL) for 30 min. The inks were then agitated with an ultrasonic processor (Misonix XL-2000) before casting onto a 0.05 μm Al_2O_3-polished glassy carbon electrode (Pine Research Instrumentation, diameter = 5 mm) and dried under an infrared heat lamp. The loading of the active material was 0.128 mg cm^{-2}.

In the ORR region (0 to -0.8 V *vs*. SCE), all tests were conducted in O_2-saturated 0.1 M KOH solution. Glassy carbon electrodes loaded with the catalysts were first scanned with cyclic voltammetry (CV) at 30 mV s^{-1} for several cycles prior to the linear

sweep voltammetry (LSV). LSV measurements at 10 mV s^{-1} were scanned and recorded at rotation speeds ranging from 400 rpm to 1600 rpm. The number of electrons transferred at -0.8 V vs. SCE was calculated using the Koutecky-Levich equation.

In the OER region (0 V to 0.8 V *vs*. SCE), all tests were conducted in N_2-saturated KOH solutions with varying concentrations. LSV (1 mV s^{-1}) and CV (30 mV s^{-1}) measurements were obtained with a rotation speed of 2000 rpm. Prior to the LSV scan, for Co_3O_4, the physical mixture of $Co_3O_4$and CNW, and the Co_3O_4/CNW, the electrodes were cycled for three cycles. For CNW, the electrodes were cycled once. IR compensation was applied using the resistance obtained by AC impedance prior to the calculation of the Tafel slope and reaction order. The reaction order (*m*) with respect to the OH- activity was obtained by calculating the slope of the plot log i (i = current density) *vs*. log a_{OH^-} (a_{OH^-} = activity of the hydroxide), respectively, at potentials of 0.58 V and 0.60 V *vs*. SCE. The stability of catalysts was studied by cycling the electrodes in various concentrations of KOH for ten cycles and calculating the current retention. Current retention was calculated by dividing the peak current at 0.8 V *vs*. SCE of the 10th cycle by that of the 1st cycle. Chronopotentiometry measurements were recorded at two current densities: 3 mA cm^{-2} in 0.1 M KOH solution and 10 mA cm^{-2} in 1 M KOH solution.

3.3 Result and Discussion

3.3.1 Catalyst Synthesis and Characterization

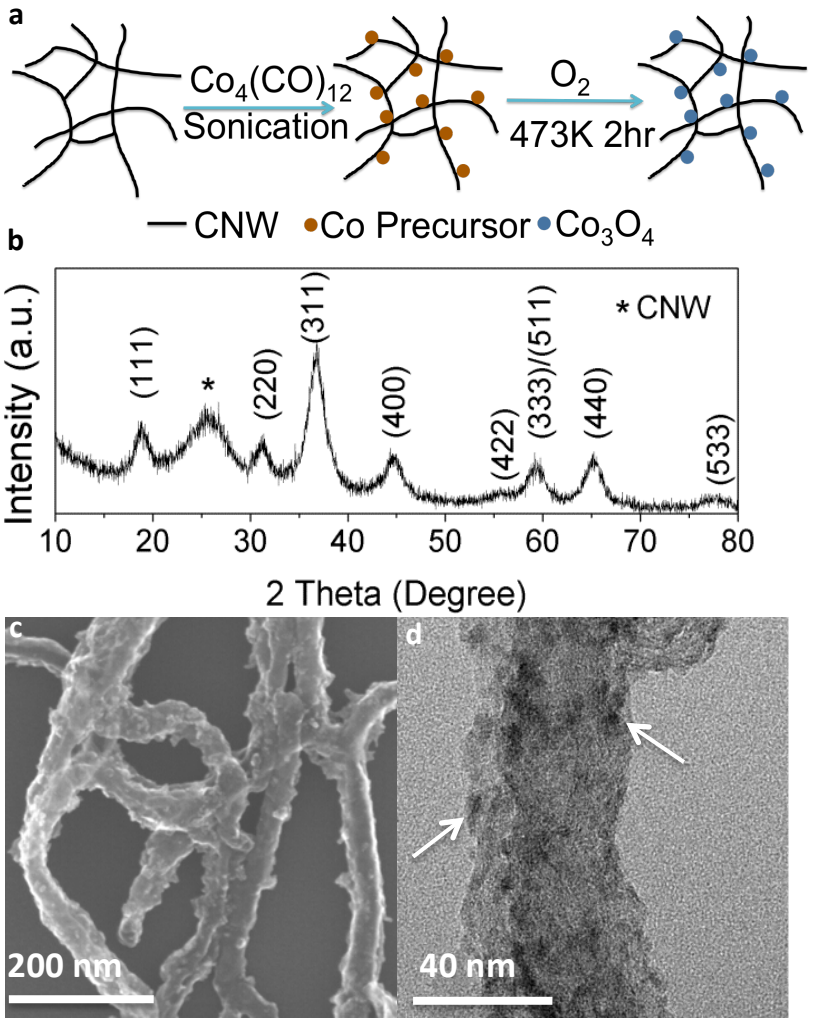

Figure 3.1: (a) Schematic pathway for the ultrasonic synthesis of Co_3O_4/CNW. (b) X-ray diffraction pattern of Co_3O_4/CNW-C. (c) Scanning Electron Microscopy image of Co_3O_4/CNW-C. (d) High Resolution Transmission Electron Microscopy image of Co_3O_4/CNW-C.

The *in situ* growth of Co_3O_4 on CNW (Co_3O_4/CNW) was achieved by an ultrasonic method followed by controlled heat treatment (see schematic pathway in Fig.

3.1a).[42-44] The synthesis involved two steps: Co precursor nanoparticles assembling on the surface of CNW during the sonication process followed by heating the powder in air at 473 K for 2 h to obtain Co_3O_4/CNW. To study the relationship between Co_3O_4 loading and the catalytic activities of the composite materials, we prepared the Co_3O_4/CNW samples with three different Co_3O_4 loadings denoted, respectively, as Co_3O_4/CNW-A, Co_3O_4/CNW-B and Co_3O_4/CNW-C. The Co_3O_4 loadings were measured with thermogravimetric analysis (TGA) (see Fig. 3.2). The loadings of Co_3O_4 on Co_3O_4/CNW-A, Co_3O_4/CNW-B and Co_3O_4/CNW-C are, respectively, 21.9%, 29.8%, and 41.5%. TGA analysis also demonstrates that with increased loading of Co_3O_4, the temperature of carbon combustion is lowered. This suggests that the presence of Co_3O_4 catalyzes the combustion of the CNW. The second weight loss for Co_3O_4/CNW-B and Co_3O_4/CNW-C is probably due to the combustion of carbon not directly connected to Co_3O_4.[45,46]

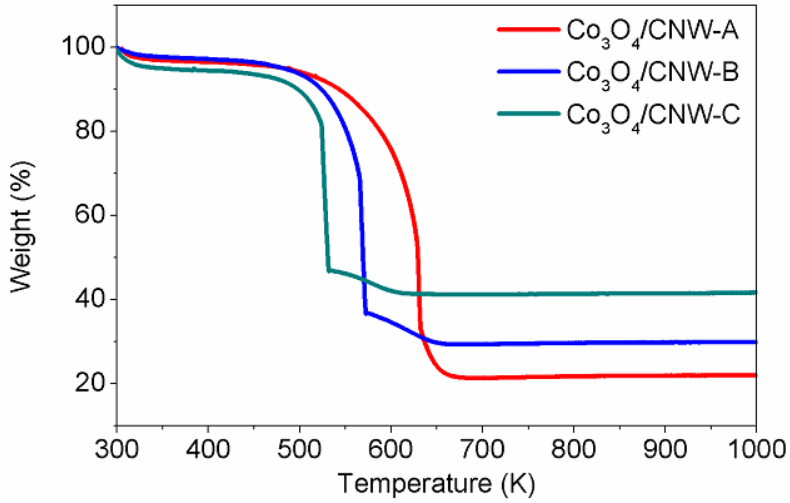

Figure 3.2: Thermogravimetric analysis of Co_3O_4/CNW.

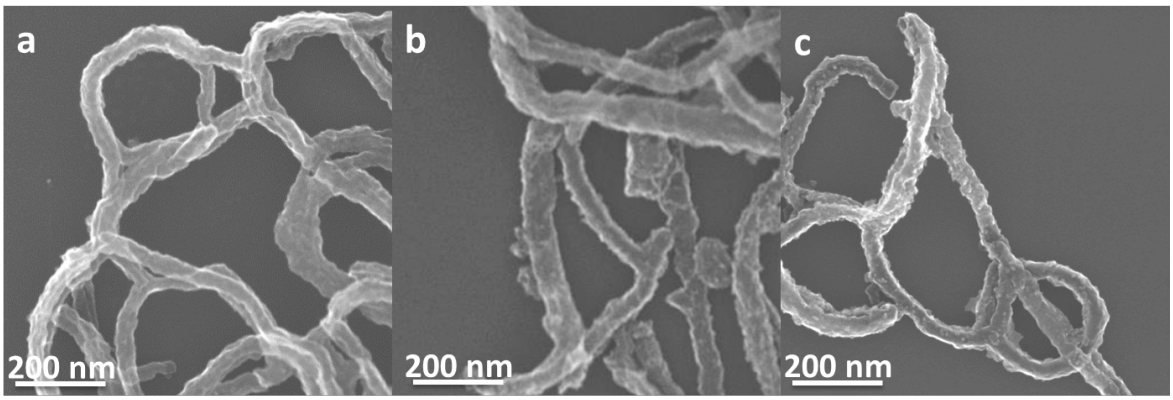

Figure 3.3: SEM images of (a) Co_3O_4/CNW-A, (b) Co_3O_4/CNW-B, and (c) Co_3O_4/CNW-C.

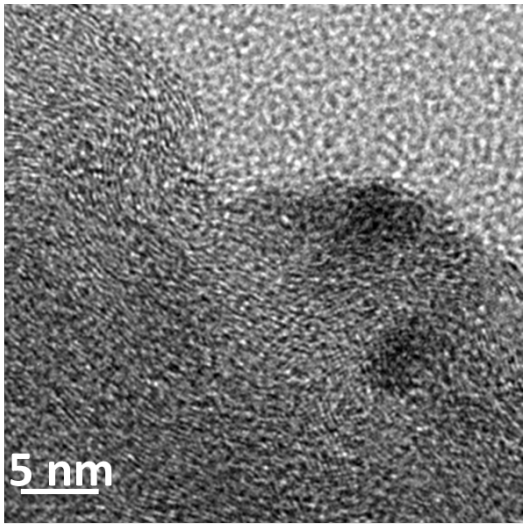

Figure 3.4: High-resolution TEM image of Co_3O_4/CNW-C.

Fig. 3.1b shows the characteristic X-ray diffraction (XRD) pattern of Co_3O_4/CNW, with the major peaks indexed to spinel Co_3O_4. The additional broad peak from 20° to 30°can be attributed to CNW.[22] The absence of Co or CoO peaks suggest that all of the Co precursor is successfully oxidized to Co_3O_4.[43] The size and morphology of the Co_3O_4/CNW were characterized with scanning electron microscopy (SEM) and transmission electron microscopy (TEM). As shown in Fig. 3.1c and d, and Fig. 3.3 and

3.4, the Co_3O_4nanoparticles are well dispersed on the surface of CNW with a particle size close to 5 nm. The small particle size of the Co_3O_4 can be attributed to the low reaction temperature of the ultrasonic synthesis. This demonstrates that *in situ* synthetic methods are advantageous in preparing composites with well-dispersed and small-sized particles which are beneficial for catalysis. The gas-adsorption surface areas of CNW, Co_3O_4/CNW-A, Co_3O_4/CNW-B, and Co_3O_4/CNW-C are, respectively, 161, 166, 160, and 121 $m^2 g^{-1}$ (see Fig. 3.5).

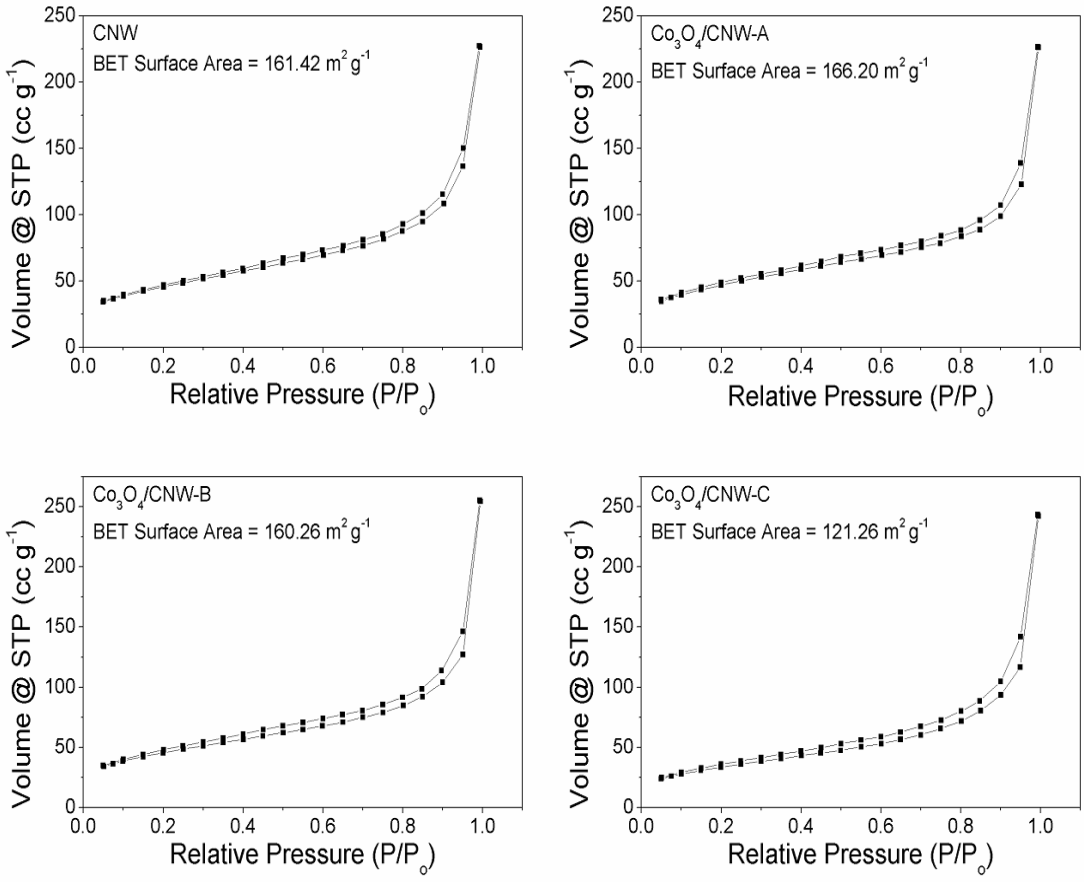

Figure 3.5: Brunner-Emmett-Teller (BET) isotherms of CNW and Co_3O_4/CNW composite materials.

3.3.2 Oxygen Reduction Reaction

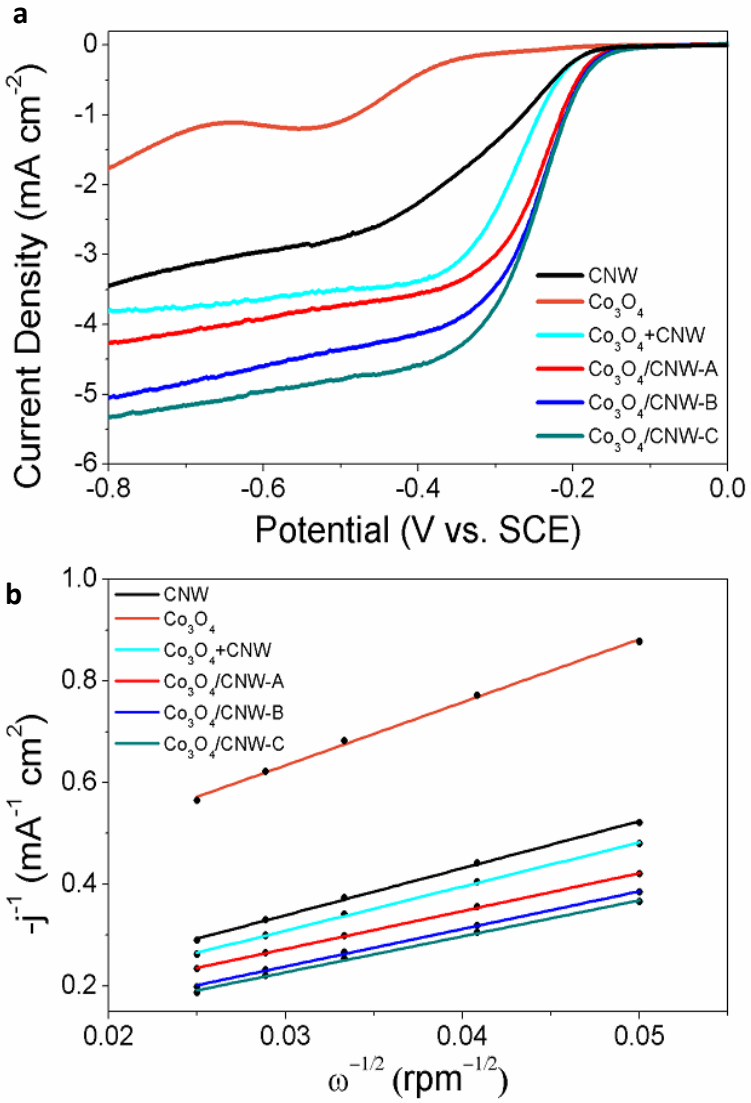

Figure 3.6: (a) Rotating disk electrode voltammograms at 1600 rpm from 0 to -0.8 V *vs*. SCE, and (b) Koutecky-Levich plots at -0.8 V *vs*. SCE.

The ORR activities of the catalysts were studied by LSV from 0 to -0.8 V *vs*. SCE at 10 mV s^{-1} and the number of electrons transferred was calculated from the Koutecky-Levich equation (see Fig. 3.6 and Fig. 3.7). The onset potential of Co_3O_4 is much more negative than those of the other catalysts. The number of electrons transferred for Co_3O_4

is 2.27 at -0.8 V *vs*. SCE, suggesting a predominant two-electron pathway for ORR. However, as the Co_3O_4 does not reach a mass transfer limitation, the uncertainty in the obtained figure is probably larger than that for other samples. For CNW, the onset potential is ~ -0.2 V *vs*. SCE with the number of electrons transferred being around 3.05 at -0.8 V *vs*. SCE. The physical mixture (Co_3O_4 + CNW) exhibits a similar onset potential of ~ -0.2 V *vs*. SCE and the number of electrons transferred is 3.30 at -0.8 V *vs*. SCE. The onset potentials for Co_3O_4/CNW-A, Co_3O_4/CNW-B, and Co_3O_4/CNW-C are all at ~ -0.15 V *vs*. SCE, with slight differences in the number of electrons transferred. These numbers at -0.8 V *vs*. SCE are, respectively, 3.79, 3.82 and 3.98, demonstrating that the ORR on the Co_3O_4/CNW catalyst favors a four-electron pathway.

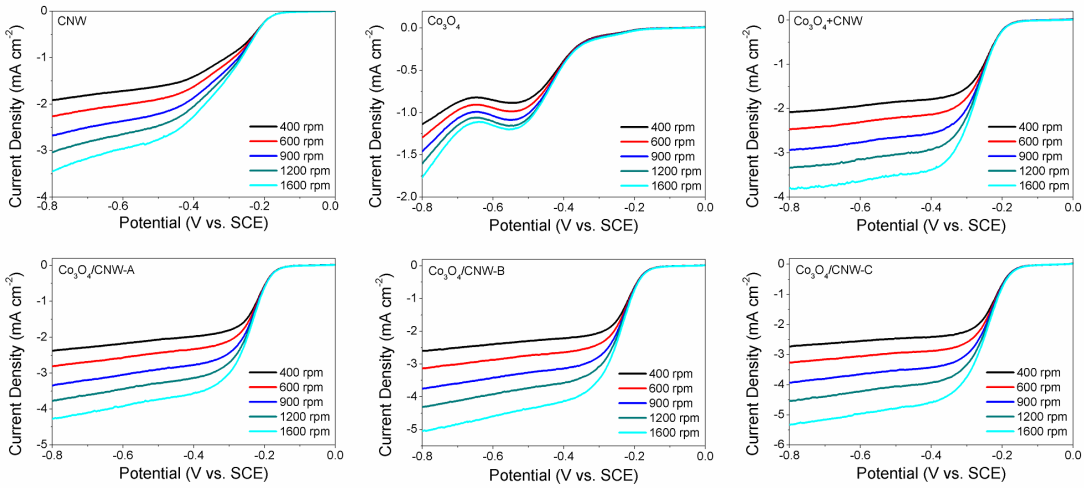

Figure 3.7: Linear voltammograms of catalysts cast onto a rotating disk electrode at various rotation speeds from 0 to -0.8 V *vs*. SCE.

Around the onset potential region, the slow reaction rate of the ORR means that O_2 provision is sufficient and the reaction rate is mainly determined by the activities of the catalysts. Thus, by analyzing the voltammogram around the onset potential region and

in the mass-transfer-limit region, one can gain insight into the activities of the catalyst materials. The onset potentials of CNW and Co_3O_4 + CNW are found to be similar and less cathodic than the onset potential of Co_3O_4. Additionally, the current densities of CNW and Co_3O_4 + CNW in the mass-transfer-limit region (-0.4 V to -0.8 V *vs*. SCE) are higher than that of pure Co_3O_4. Since Co_3O_4, with the number of electrons transferred being 2.27, acts as a poor catalyst for ORR, CNW is most likely the primary catalyst for ORR. It is worth noting that Co_3O_4 + CNW shows similar catalytic activity as CNW near the onset potential region but exhibits higher current density in the mass-transfer-limit region with a higher number of electrons transferred. This suggests that the presence of Co_3O_4 in the physical composite facilitates the four-electron ORR pathway over the two-electron pathway.

It is of interest to compare the performance of Co_3O_4/CNW-C and Co_3O_4 + CNW due to the similar loadings of Co_3O_4 and CNW in them. As shown in Fig 3.6, Co_3O_4/CNW-C exhibits a more positive onset potential with higher current density in the mass-transfer-limit region and more electrons transferred, demonstrating a better ORR catalytic activity of the *in situ*-grown sample. The improvement in the catalytic actitivies of the *in situ*-grown samples is not simply because of the enhanced conductivity between Co_3O_4 and CNW, but more importantly due to the coupling effect between Co_3O_4 and CNW.[11,12] Co_3O_4/CNW-A, Co_3O_4/CNW-B and Co_3O_4/CNW-C all exhibit similar onset potentials while the number of electrons transferred increases as the loading of Co_3O_4 increases, further suggesting that Co_3O_4 assists in catalyzing ORR via a selective four-electron process when coupled with CNW.

3.3.3 Oxygen Evolution Reaction

(1) OER Activities

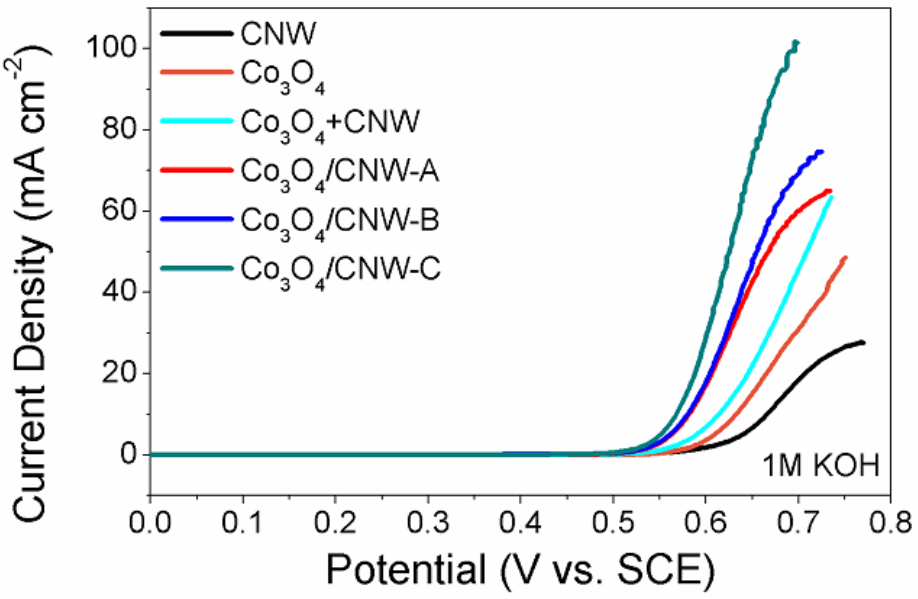

Figure 3.8: Rotating disk electrode voltammograms after iR correction from 0 to 0.8 V *vs*. SCE in 1 M KOH solution. Rotation speed was 2000 rpm.

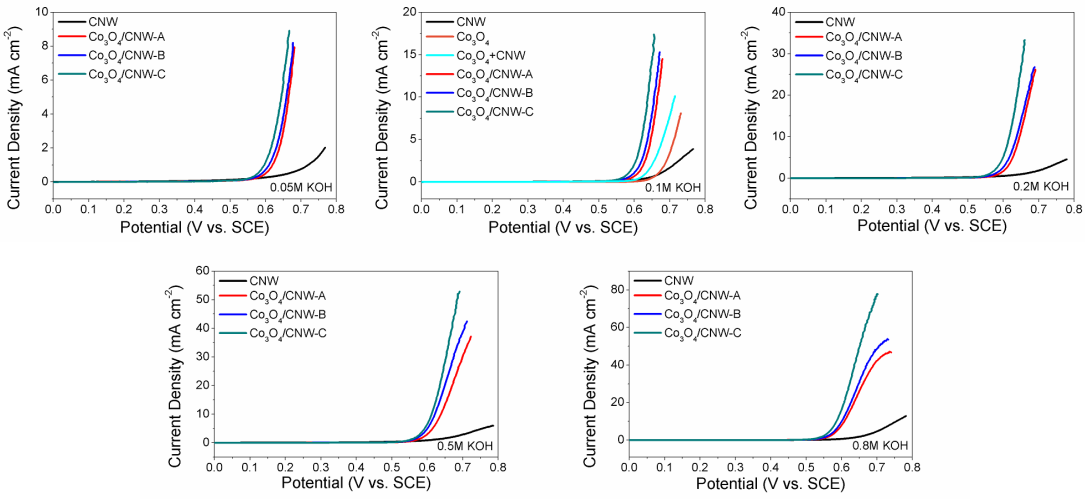

Figure 3.9: Rotating disk electrode voltammograms after iR correction at 2000 rpm from 0 to 0.8 V *vs*. SCE in different concentrations of KOH solutions.

The OER catalytic activities of the catalysts were studied by LSV from 0 to 0.8 V *vs*. SCE at 1 mV s^{-1} in KOH solutions of various concentrations (see Fig. 3.8 and Fig. 3.9). As shown in Fig. 3.8, the onset potential for CNW is ~ 0.57 V *vs*. SCE and the peak current density is ~ 28 mA cm^{-2} in a 1 M KOH solution. The onset potential for Co_3O_4 is ~ 0.56 V *vs*. SCE and the peak current density is ~ 49 mA cm^{-2}. For Co_3O_4 + CNW, the onset potential is ~ 0.52 V *vs*. SCE and the peak current density is ~ 63 mA cm^{-2}. The onset potentials for Co_3O_4/CNW-A, Co_3O_4/CNW-B and Co_3O_4/CNW-C, are all ~ 0.50 V *vs*. SCE and the current densities are 65, 75 and 102 mA cm^{-2}, respectively. At high potentials, the voltammograms of samples containing CNW exhibit a plateau. This is probably due to the degradation of carbon at high potentials, especially in the higher concentration KOH solution, which will be discussed later.

CNW exhibits poorer OER catalytic activity compared to the Co_3O_4-containing samples, indicating that CNW is not a good OER catalyst and that Co_3O_4 serves as the primary catalytic site for the OER. It is worth noting that the degradation of carbon might also contribute to the apparent current of CNW, which will be discussed later. In comparing the performance of Co_3O_4 + CNW with pure Co_3O_4, Co_3O_4 + CNW exhibits a lower onset potential and higher current density despite containing only 40 wt.% Co_3O_4, demonstrating improved OER catalytic activity in the presence of CNW. This improvement is probably due to the 3D conductive network of CNW, which connects Co3O4 particles with the current collector, allowing improved electron transfer.

The differences among the OER onset potentials of Co_3O_4/CNW-A, Co_3O_4/CNW-B, and Co_3O_4/CNW-C are found to be small despite the differences in the amount of Co_3O_4 loaded onto the materials. Also, despite the similar Co_3O_4 loading in Co_3O_4/CNW-C and Co_3O_4 + CNW, Co_3O_4/CNW-C exhibits a lower onset potential and a much higher current density (102 mA cm^{-2} compared to 63 mA cm^{-2}), indicating better OER catalytic

activity of the *in situ*-grown samples. This is due to the synergistic coupling effect between Co_3O_4 and CNW, occurring as part of the *in situ* growth. Because both Co_3O_4/CNW-C and Co_3O_4 + CNW exhibit similar levels of Co_3O_4 dispersity in the 3D carbon network (Fig. 3.3), the enhanced current density most likely arises from the improved electron transfer due to the coupling of CNW and Co_3O_4 in the Co_3O_4/CNW-C sample. Additionally, the peak current density of Co_3O_4/CNW-A, Co_3O_4/CNW-B and Co_3O_4/CNW-C increases as the loading of Co_3O_4 increases, further confirming that Co_3O_4 is the primary catalyst for the OER when coupled with a carbon support.

(2) OER Stability

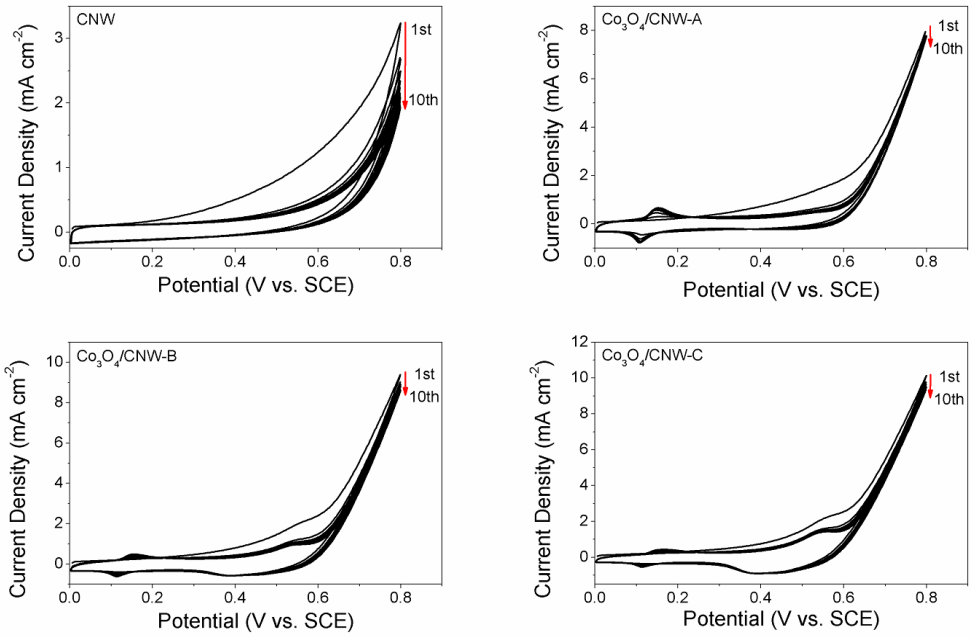

Figure 3.10: Cyclic voltammograms in N_2-saturated 0.05 M KOH from 0 to 0.8 V *vs.* SCE.

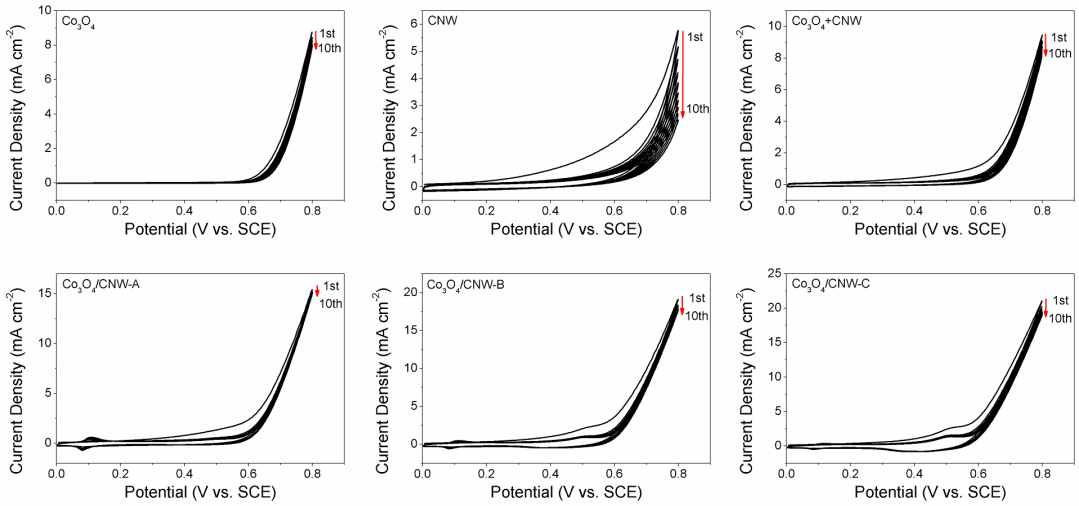

Figure 3.11: Cyclic voltammograms in N_2-saturated 0.1 M KOH from 0 to 0.8 V *vs*. SCE.

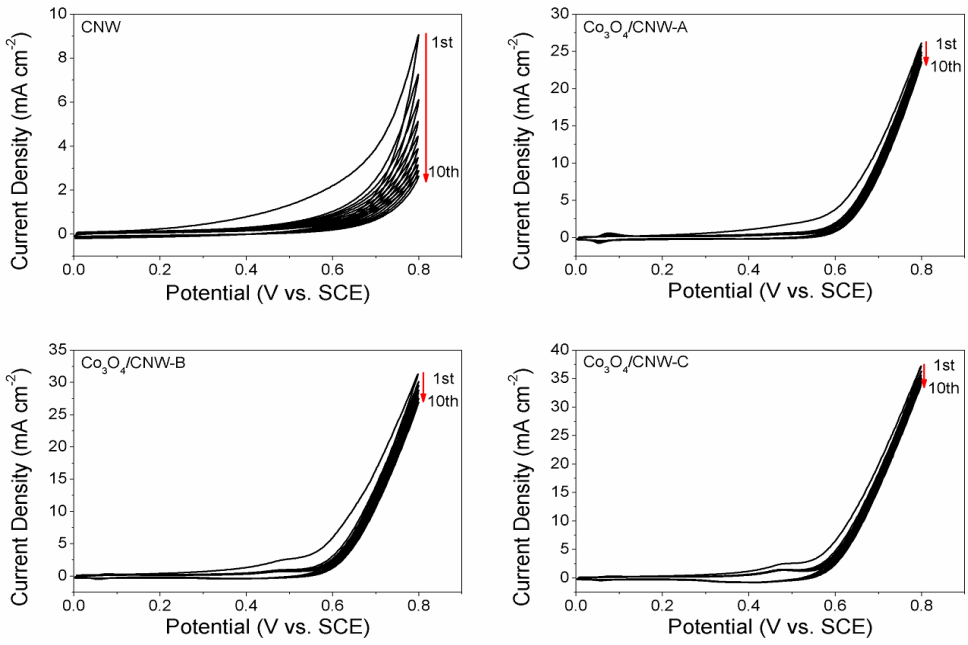

Figure 3.12: Cyclic voltammograms in N_2-saturated 0.2 M KOH from 0 to 0.8 V *vs*. SCE.

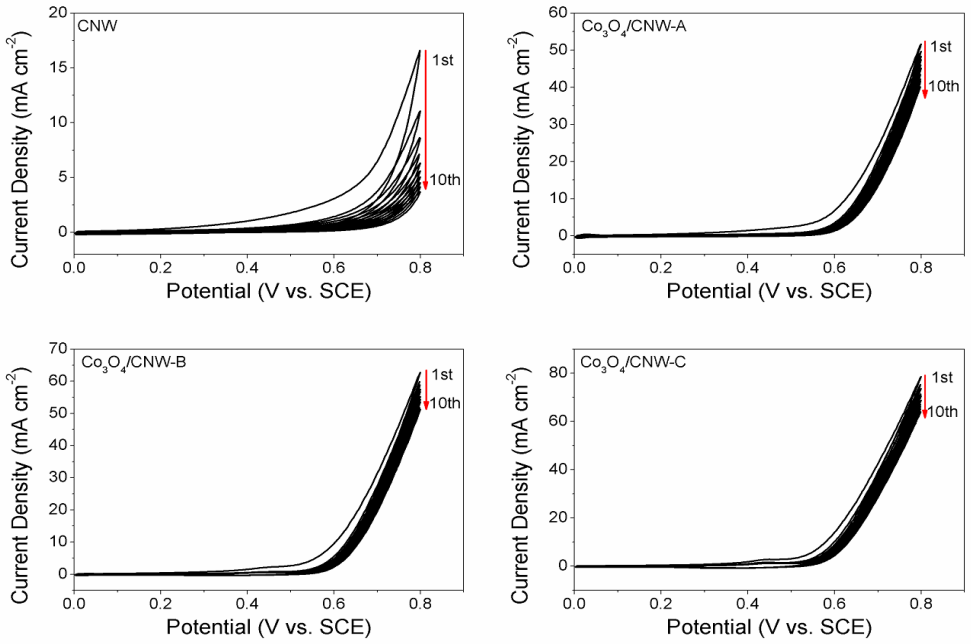

Figure 3.13: Cyclic voltammograms in N_2-saturated 0.5 M KOH from 0 to 0.8 V *vs*. SCE.

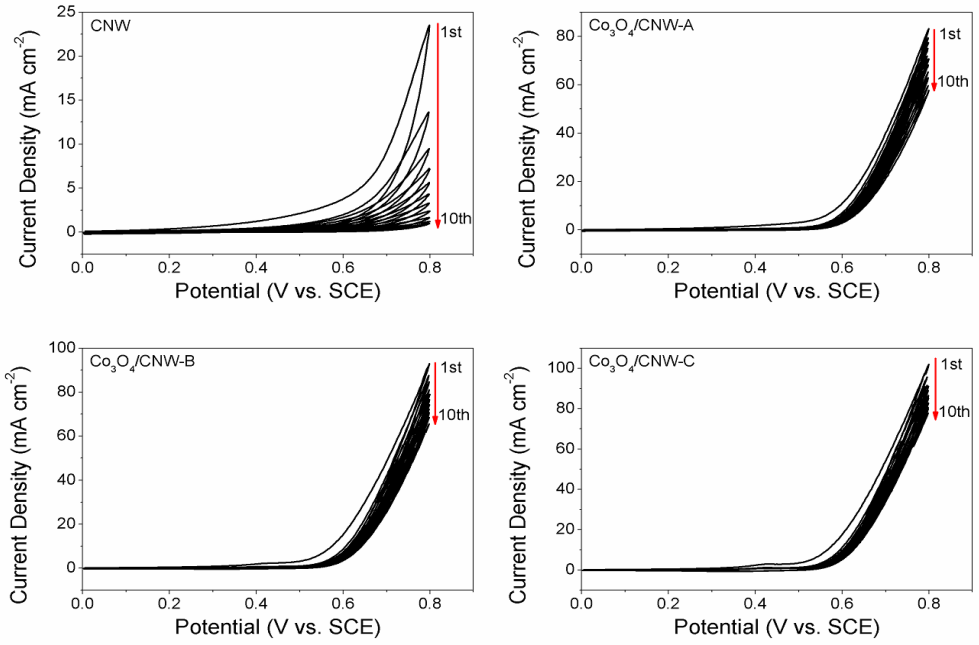

Figure 3.14: Cyclic voltammograms in N_2-saturated 0.8 M KOH from 0 to 0.8 V *vs*. SCE.

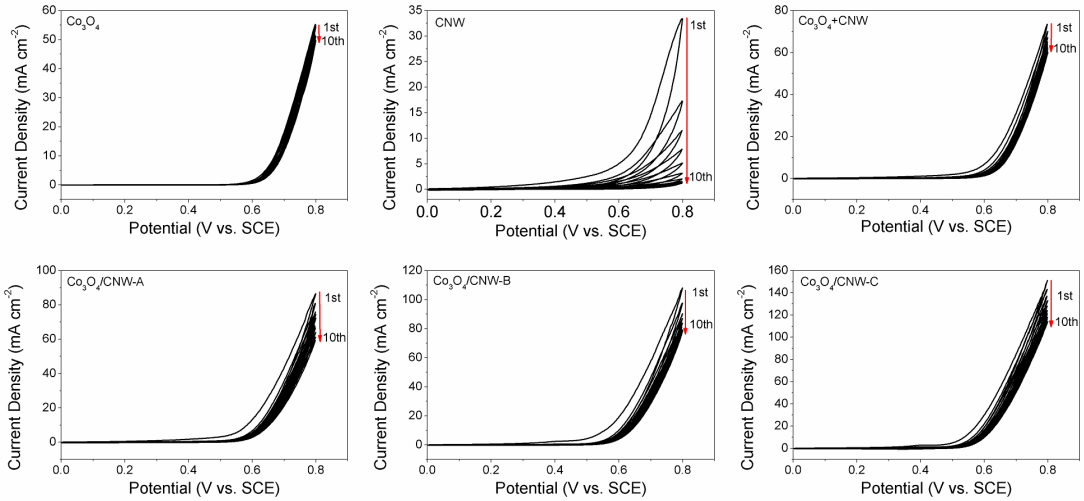

Figure 3.15: Cyclic voltammograms in N_2-saturated 1 M KOH from 0 to 0.8 V *vs*. SCE.

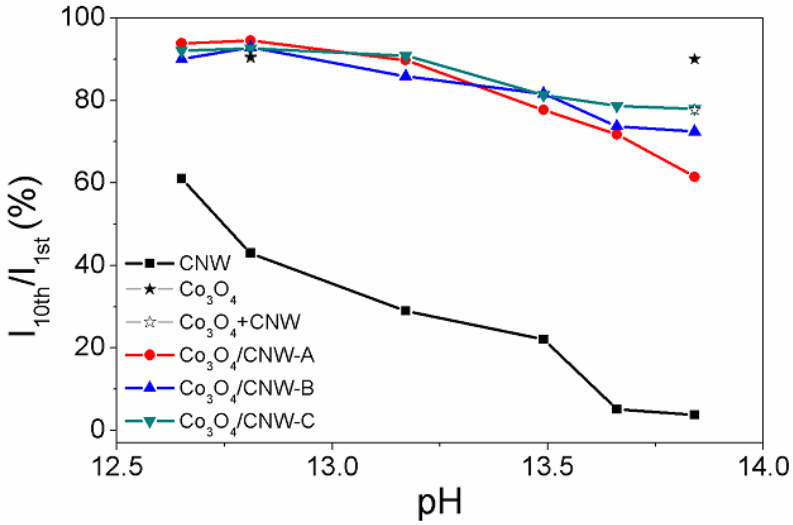

Figure 3.16: Current retention of the 10th cycle at 0.8 V *vs*. SCE with respect to the 1st cycle for catalysts in electrolytes with varying pH values of KOH solutions.

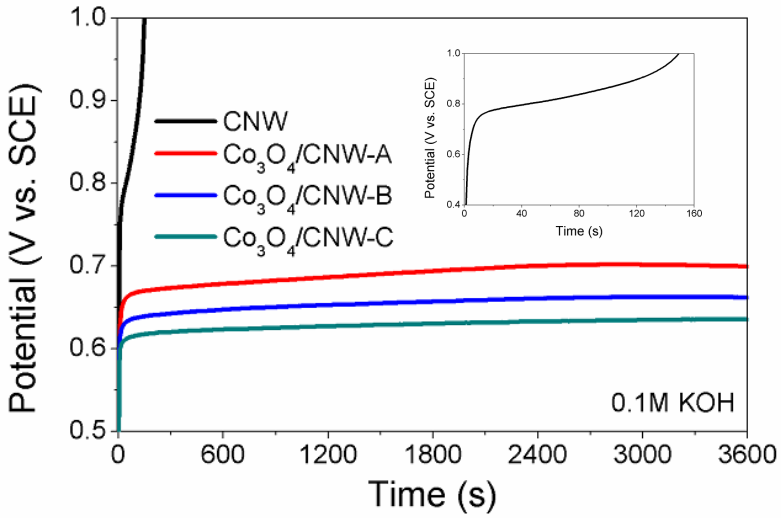

Figure 3.17: Chronopotentiometry curves of CNW and Co_3O_4/CNW catalysts on rotating disk electrodes at a constant current density of 3 mA cm^{-2} in 0.1 M KOH solution. The inset shows an amplification of the chronopotentiometry curve of CNW.

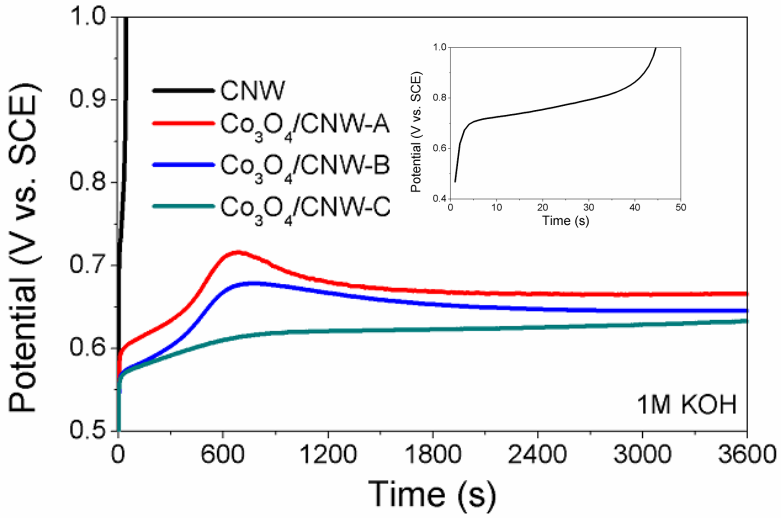

Figure 3.18: Chronopotentiometry curves of CNW and Co_3O_4/CNW catalysts on rotating disk electrodes at a constant current density of 10 mA cm^{-2} in 1 M KOH solution. The inset shows an amplification of the chronopotentiometry curve of CNW.

The lifetime of rechargeable batteries is an important aspect for their practical use, so the stability of the catalysts is of great importance. Accordingly, the stabilities of the catalysts were studied by cyclic voltammetry and chronopotentiometry (see Fig. 3.10 ~ 3.15, Fig. 3.17 and Fig. 3.18). The current of the 10th cycle at 0.8 V *vs*. SCE with respect to that of the 1st cycle was calculated and is shown in Fig. 3.16. It is evident that CNW degrades rapidly, especially in the high concentration hydroxides. The current retention of CNW in 1 M KOH solution is ~ 3% while it is ~ 62% in 0.1 M KOH. The current retention of pure Co_3O_4 is very similar in both 0.1 M and 1 M KOH solutions (~ 91%), indicating that Co_3O_4 is stable in the OER potential region across KOH concentrations. For Co_3O_4/CNW-A, Co_3O_4/CNW-B and Co_3O_4/CNW-C, their current retentions are very similar in low concentration KOH solution (~ 90%). But as the pH increases, the catalysts with higher Co_3O_4 loadings exhibit better stability. The current retentions of the samples with similar Co_3O_4 loading (Co_3O_4/CNW-C and Co_3O_4 + CNW) are very similar in both 0.1 and 1 M KOH solutions, suggesting that the degradation of the catalysts is mainly due to CNW. But with higher Co_3O_4 loadings, the catalysts demonstrate better stability in the OER potential region, suggesting that Co_3O_4 assists in suppressing the degradation of CNW. Chronopotentiometry curves of CNW and Co_3O_4/CNW catalysts in 0.1 and 1 M KOH solutions also confirm that the catalytic activities and stabilities of catalysts improve as the loading of Co_3O_4 increases (see Fig. 3.17 and Fig. 3.18).

There are two possible mechanisms through which Co_3O_4 improves the overall stability of the catalysts in the OER potential region: The first being that Co_3O_4 physically blocks the contact of CNW with KOH and the oxygen bubbles formed on Co_3O_4 expel KOH solution away from carbon so that the degradation is suppressed. The second mechanism is that there is a competition between OER and carbon degradation in the

oxidizing potential region on the surface of the catalysts. By lowering the activation barrier and improving the reaction kinetics of OER, there is a preference for OER over the decomposition of carbon so that the overall stability of the catalysts is improved. As observed in the SEM and TEM images, CNW is never fully blocked by Co_3O_4 (even at higher Co_3O_4 loading) and thus is accessible to OH^-. Also, as the samples containing Co_3O_4 exhibit better catalytic activities (lower onset potentials and higher current densities), the second explanation is probably the dominant mechanism that suppresses the degradation of CNW.

(3) Tafel Slope

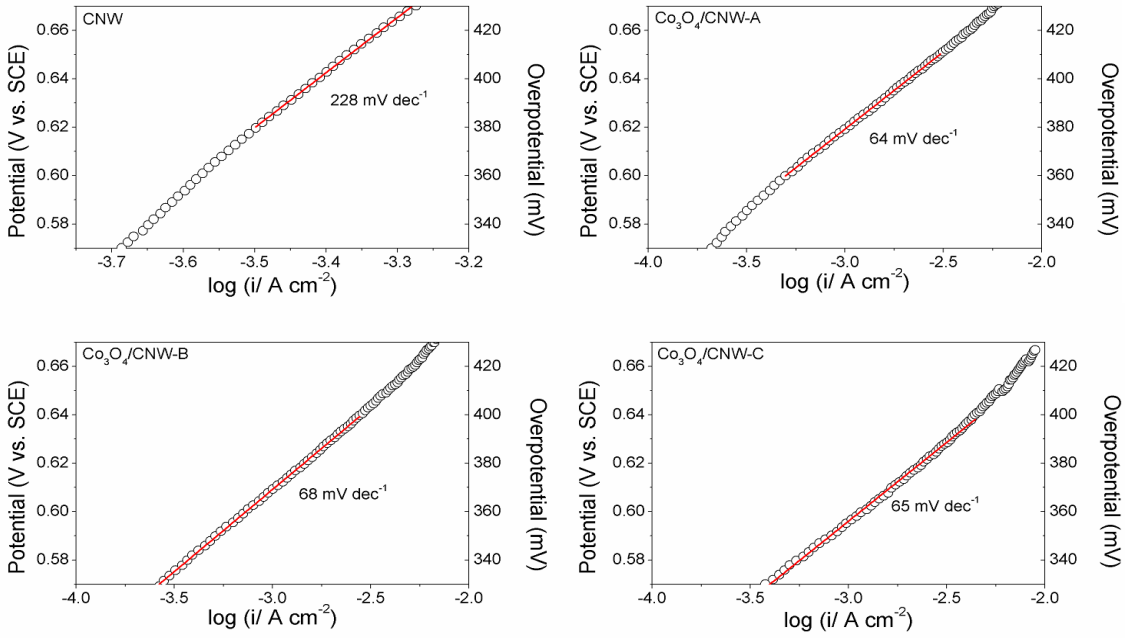

Figure 3.19: Tafel plots of catalysts loaded onto a glassy carbon electrode recorded at 1 mV s^{-1} in 0.05 M KOH.

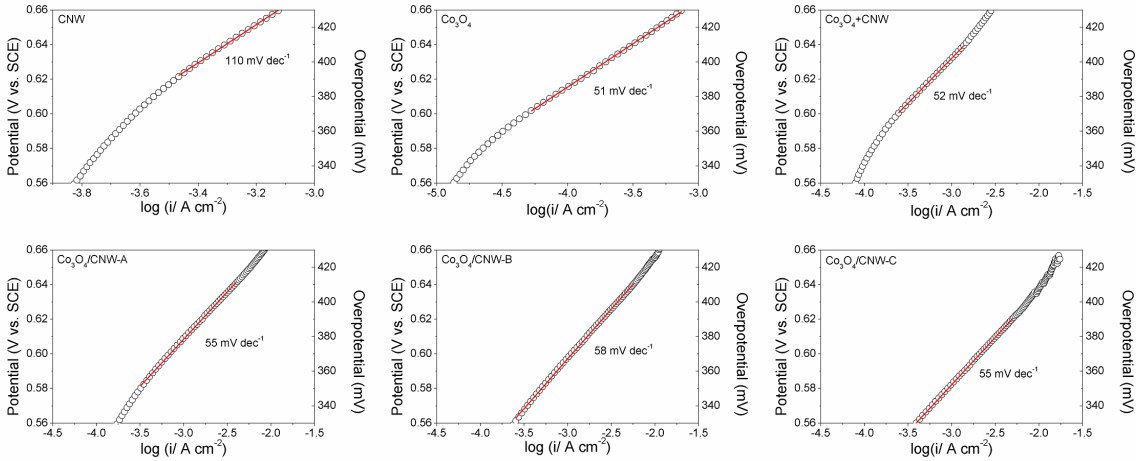

Figure 3.20: Tafel plots of catalysts loaded onto a glassy carbon electrode recorded at 1 mV s^{-1} in 0.1 M KOH.

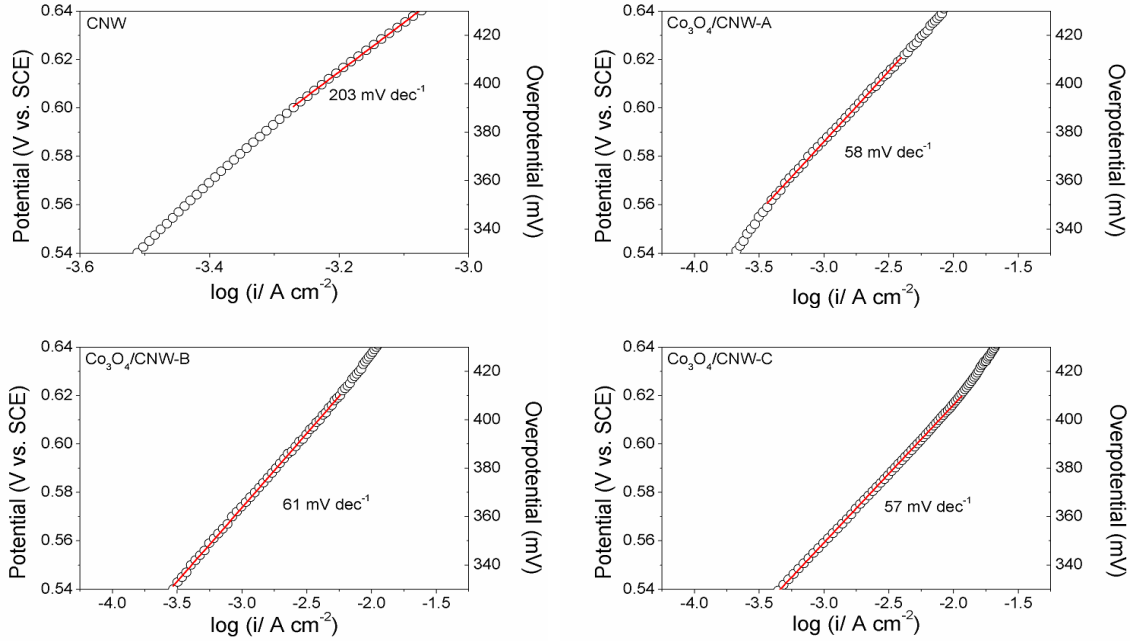

Figure 3.21: Tafel plots of catalysts loaded onto a glassy carbon electrode recorded at 1 mV s^{-1} in 0.2 M KOH.

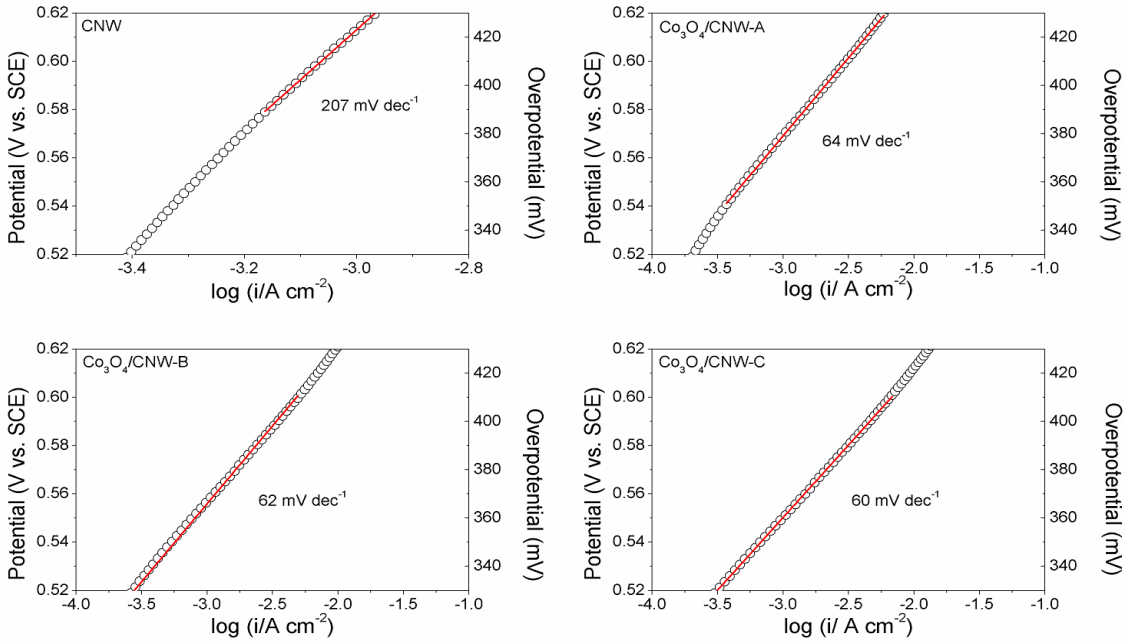

Figure 3.22: Tafel plots of catalysts loaded onto a glassy carbon electrode recorded at 1 mV s^{-1} in 0.5 M KOH.

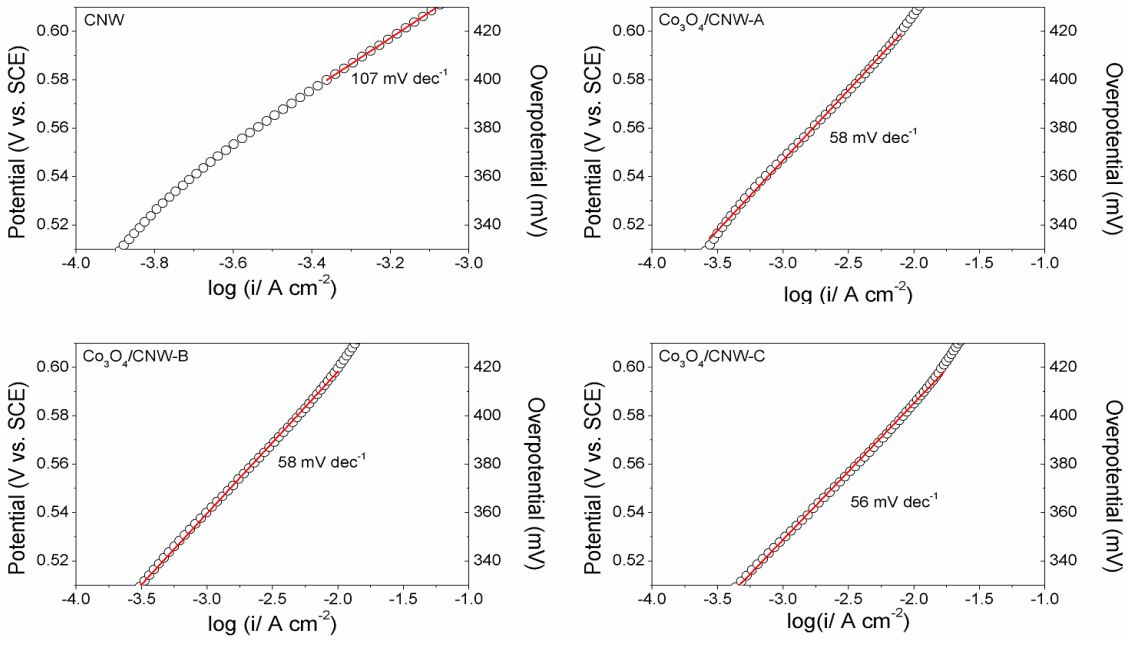

Figure 3.23: Tafel plots of catalysts loaded onto a glassy carbon electrode recorded at 1 mV s^{-1} in 0.8 M KOH.

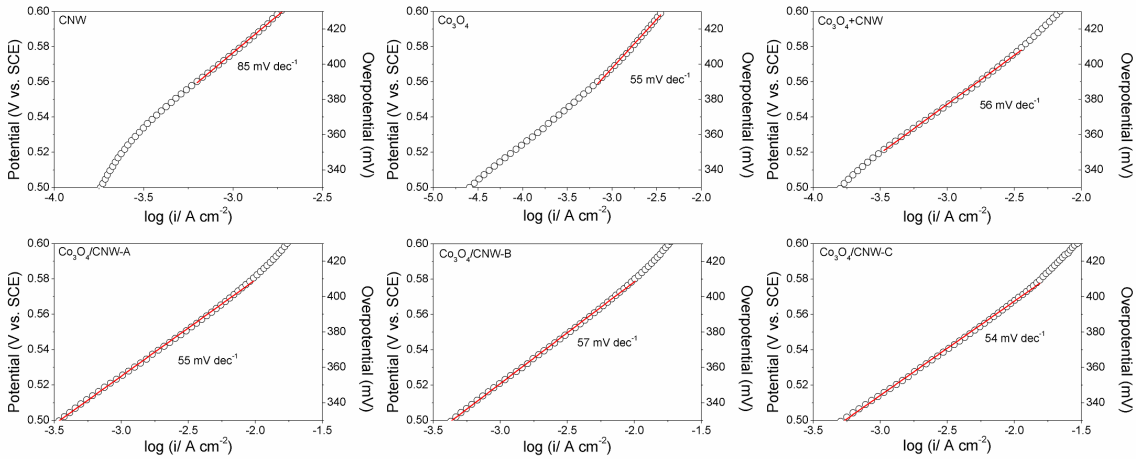

Figure 3.24: Tafel plots of catalysts loaded on a glassy carbon electrode recorded at 1 mV s^{-1} in 1 M KOH.

Tafel plots can provide insight into the OER mechanism on these catalysts as the slope reflects the rate-determining step of the catalytic reaction. Tafel plots in KOH solutions ranging in concentrations from 0.05 to 1 M were derived from the LSV curves with iR compensation. The Tafel plots in are shown in Fig. 3.19 ~ Fig. 3.24. The Tafel slope of each catalyst beyond the onset potential was calculated and is shown in the plots. Different from the pure CNW catalyst, all samples containing Co_3O_4 have a rate determining value reflecting the characteristic Tafel slope of Co_3O_4 (~ 60 mV dec^{-1}) across KOH concentrations.[33-35] This further confirms that Co_3O_4 is the primary OER catalyst in the Co_3O_4/CNW catalyst.

(4) Reaction Order

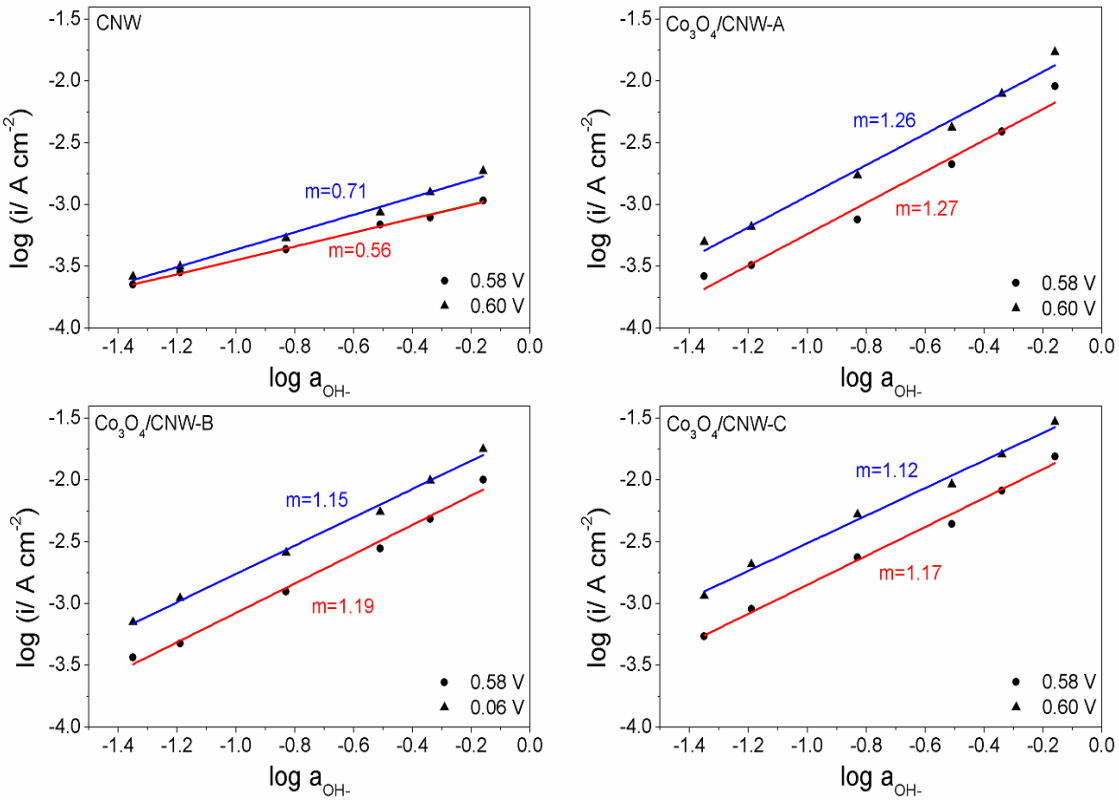

Figure 3.25: Reaction order (*m*) with respect to the activity of OH^- (a_{OH^-}) based on the polarization curves at potentials of 0.58 V and 0.60 V *vs*. SCE.

To further understand the OER mechanism of the Co_3O_4/CNW catalysts, the reaction orders (*m*) with respect to the activity of OH- at 0.58 and 0.60 V *vs*. SCE were calculated and are shown in Fig. 3.25. For CNW, the reaction order is ~ 0.56 at 0.58 V and ~ 0.71 at 0.60 V. The reaction order for Co_3O_4/CNW-A, Co_3O_4/CNW-B and Co_3O_4/CNW-C is ~ 1.2 at both potentials, similar to the reported values in the literature for pure Co_3O_4.[34,35]

The increase in the reaction order of CNW as the potential increases indicates its instability at high oxidizing potentials, while the steady reaction order of Co_3O_4/CNW

suggests a stable OER mechanism. It is likely that the change in the reaction order of CNW at the two selected potentials is due to the degradation of carbon. As the Tafel slope and reaction order of Co_3O_4/CNW all exhibit the characteristic value of Co_3O_4, it can be concluded that exclusive OER catalysis occurred on Co_3O_4. Additionally, it further suggests that the OER on Co_3O_4outcompetes the degradation of CNW, confirming that the improvement in CNW stability in the Co_3O_4/CNW is mainly due to the enhanced OER kinetics.

3.3.4 Perspective

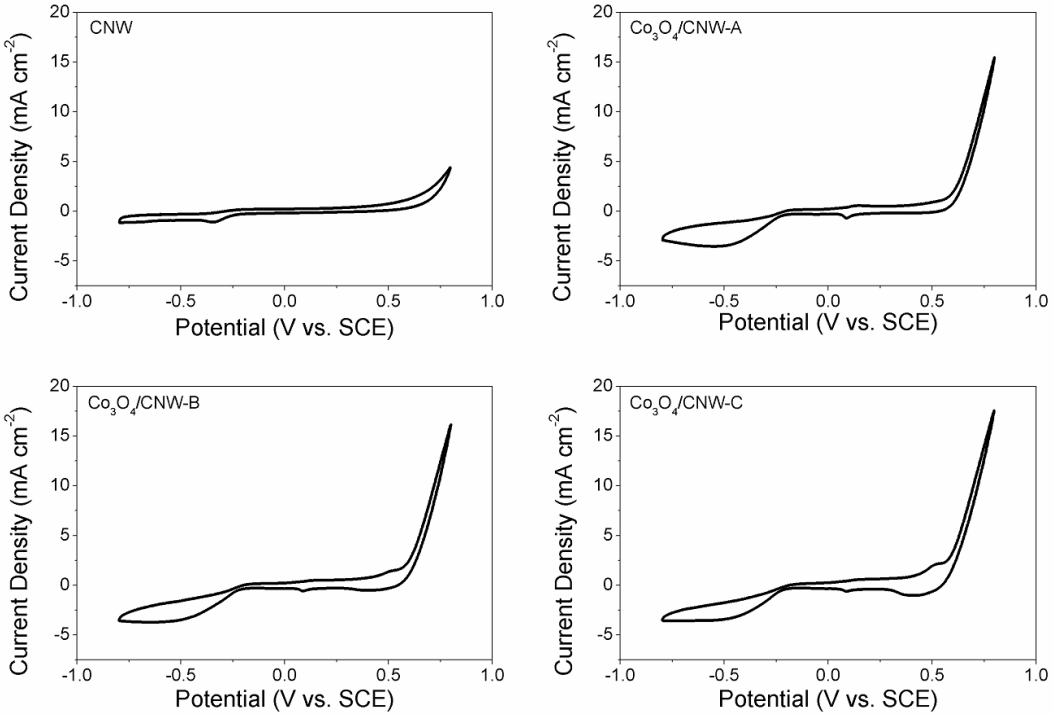

Figure 3.26: Cyclic voltammograms in N_2-saturated 0.1 M KOH from -0.8 V to 0.8 V *vs.* SCE recorded after two cycles at the scan speed of 30 mV s^{-1}.

The findings in this thesis suggest that coupling carbon materials with transition-metal oxides such as Co_3O_4 can be a promising approach for OER/ORR bifunctional catalysts in alkaline electrolytes (see Fig. 3.26). These findings also provide guidelines for future bifunctional catalyst development: (1) The *in situ* growth of transition-metal oxides can be used to obtain well-dispersed and small-sized oxide particles on a carbon support to obtain advanced bifunctional catalysts. The improved catalytic activities due to the coupling effects between the oxides and the carbon network are beneficial for both ORR and OER. (2) Carbon supports with excellent stability in alkaline solution at high potential are of key significance to ensure the desirable durability of metal-air batteries. (3) Metal oxides with good synergistic activities are of importance to reach a selective four-electron pathway for ORR. (4) Metal oxides with high OER catalytic activities are essential in their roles in catalyzing the oxidation of OH^- and stabilizing the carbon support.

3.4 Conclusion

The *in situ* growth of Co_3O_4 onto CNW was achieved through an ultrasonic method followed by a controlled heat treatment. Electrochemical investigation suggests that CNW in the composite materials is the primary catalyst for ORR while Co_3O_4 acts with CNW as a synergistic catalyst to assist the selective four-electron ORR over the two-electron process. The roles of Co_3O_4 and CNW in OER are reversed from those in the ORR. CNW improves the electron transfer between Co_3O_4 and the current collector. Co_3O_4 acts as the primary catalytic site and stabilizes CNW mainly due to the preference of OER over the degradation of CNW as a result of the improved OER kinetics. The coupling effects between Co_3O_4 and CNW can further enhance the catalytic activities of

the composite materials, both for ORR and OER. The finding suggests that research on carbon materials with higher stability under oxidizing potential and on metal oxides with better synergistic ORR catalytic activities and better OER catalytic performance should contribute to the development of bifunctional catalysts for the commercialization of metal-air batteries.

Chapter 4: *In Situ* Electrochemical Generation of 2-Dimensional Co_3O_4 Hexagonal Nanoplates as Highly Active Oxygen Evolution Catalysts*

4.1 INTRODUCTION

Recently, catalysts with 2-dimensional (2D) or 3-dimensional (3D) structures have attracted great attention.[20, 22, 47-50] By transporting reactants or products effectively, materials with 2D or 3D structure can facilitate the mass transfer between catalyst surface and bulk electrolyte and thus lower the concentration polarization of catalytic reaction. However, due to the strong bonding interaction between metal and oxygen atoms in the metal oxide lattice, metal oxides tend to form bulk materials with small surface area, which are not favorable for catalytic applications. One way to solve this problem is to use proper templates to prepare nano-sized 2D metal oxides. But the complexity and high cost make it almost impossible for scale-up production.[49, 51, 52]

Here, a facile synthesis of 2-dimensional Co_3O_4 (2D-Co_3O_4) nanoplates is reported using solvothermal-prepared CoO_x/Co as precursor. Along with the oxidation of the precursors to Co_3O_4, the 2D hexagonal structure forms during the anodic scan before the onset potential of OER. Further electrochemical tests show that 2D-Co_3O_4 exhibits excellent catalytic activity and stability probably due to the 2D structure of the nanoplates, which facilitates the mass transfer and provides abundant active sites for OER.

---

* Liu, S.; Li, L.; Patterson, N. A.; Manthiram, A. "Morphological Transformations during *In-situ* Electrochemical Generation of 2-Dimensional Co_3O_4 Hexagonal Nanoplates as an Oxygen Evolution Reaction Catalyst" Submitted to *ACS Applied Materials & Interfaces*.
S. Liu designed and carried out the experiment. L. Li and N. A. Patterson provided assistance in experimental work. A. Manthiram supervised the project. All participated in the preparation of the manuscript.

4.2 Experimental Details

4.2.1 Chemicals

Tetracobalt dodecacarbonyl ($Co_4(CO)_{12}$, 98%, Fisher Scientific), hexane (C_6H_{14}, 98.5%, Fisher Scientific), Iridium(IV) oxide (IrO_2, 99.99%, Alfa Aesar), and potassium hydroxide (KOH, 85.3%, Fisher Scientific) were purchased and used as-received.

4.2.2 CoO_x/Co Precursor Preparation

The tetracobalt dodecacarbonyl ($Co_4(CO)_{12}$, 0.385 mmol) was first dispersed in 60 mL hexanes (C_6H_{14}). After sonication for 30 min, the mixture was transferred into a 100 mL Teflon-lined stainless-steel autoclave and held at 433 K for 24 h. The precipitate was then vacuum filtered, washed with hexanes, de-ionized water and acetone, and dried at 50 °C overnight.

4.2.3 Stainless Steel Sheet Preparation

Stainless steel sheets were first cut into 1 cm × 2 cm rectangle shape and washed with acetone. The front side was partially covered with Kapton film (DuPont), leaving a 1 cm × 1 cm area to cast ink and a 1 cm × 0.3 cm area to connect clipper for electrochemical tests as shown in Fig. 4.1. The back side of the sheet was fully covered with Kapton film. The purpose of covering the sheet with Kapton film is to reduce signal from the sheet during the electrochemical measurements.

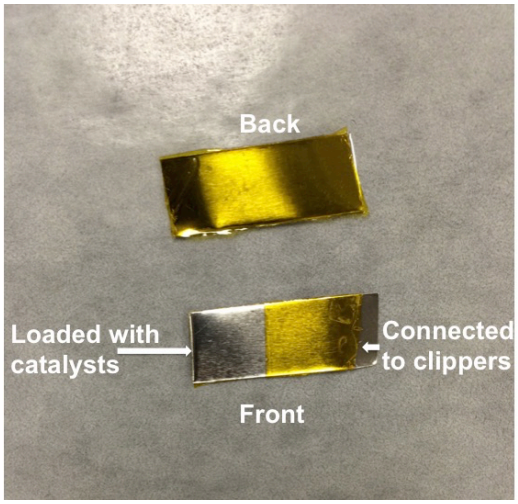

Figure 4.1: Stainless steel sheet for electrochemical measurements.

4.2.4 Ink Preparation

For electrochemical tests conducted on rotating disk electrode (RDE), the ink (denoted as ink A) was prepared by sonicating a mixture of active material (25 mg), carbon black (5 mg), a 2:1 (v/v) solution of Nafion (LQ-1105; Ion Power, Inc.) and 0.1 M NaOH (308 μL), deionized water (4 mL), and isopropanol (1 mL) for 30 min. For electrochemical tests conducted on 1 cm × 2 cm stainless steel sheet (see Figure S1), the ink (denoted as ink B) was prepared by sonicating a mixture of active material (25 mg), deionized water (4 mL), and isopropanol (1 mL) for 30 min. Before casting on RDE or stainless steel sheet, all inks were further agitated with an ultrasonic processor (Misonix XL-2000).

4.2.5 Electrochemical Measurements

All electrochemical tests were conducted in O_2-saturated 1 M KOH solution at room temperature. A saturated calomel electrode (SCE) was used as the reference electrode and platinum mesh was used as the counter electrode. To prepare rotating disk electrode, 5 μL of the ink A was drop-cast onto a 0.05 μm Al_2O_3-polished glassy carbon electrode (Pine Research Instrumentation, diameter = 5 mm) and dried under an infrared heat lamp. To prepare the sheet electrode, 25 μL of the ink B was drop-cast onto the stainless steel sheet and dried under an infrared heat lamp. Cyclic voltammetry (CV) and linear sweep voltammetry (LSV) were conducted at 30 mV s^{-1} and 1 mV s^{-1}, respectively. For RDE tests, the rotation speed was 2000 rpm. IR compensation was applied using the resistance obtained by AC impedance.

4.3 RESULT AND DISCUSSION

4.3.1 Catalyst Synthesis and Characterization

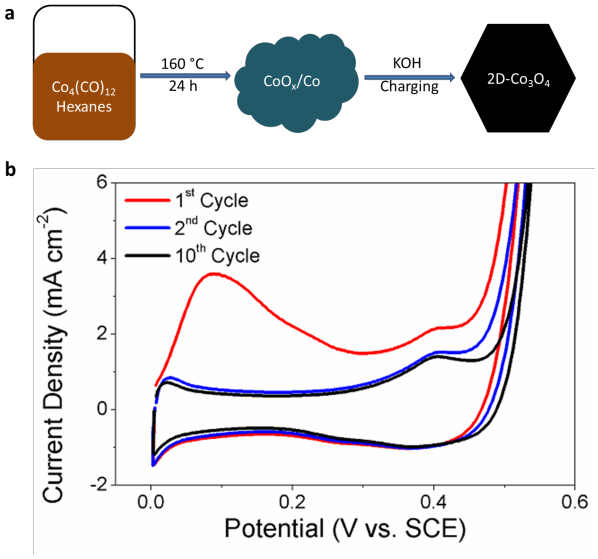

Figure 4.2: (a) Schematic pathway for the solvothermal preparation of CoO_x/Co precursors and the *in situ* generation of 2D-Co_3O_4. (b) Cyclic voltammograms of the catalyst material cast onto a rotating disk electrode after iR correction in 1 M KOH solution. The scan rate was 30 mV s^{-1} and the rotation speed was 2000 rpm.

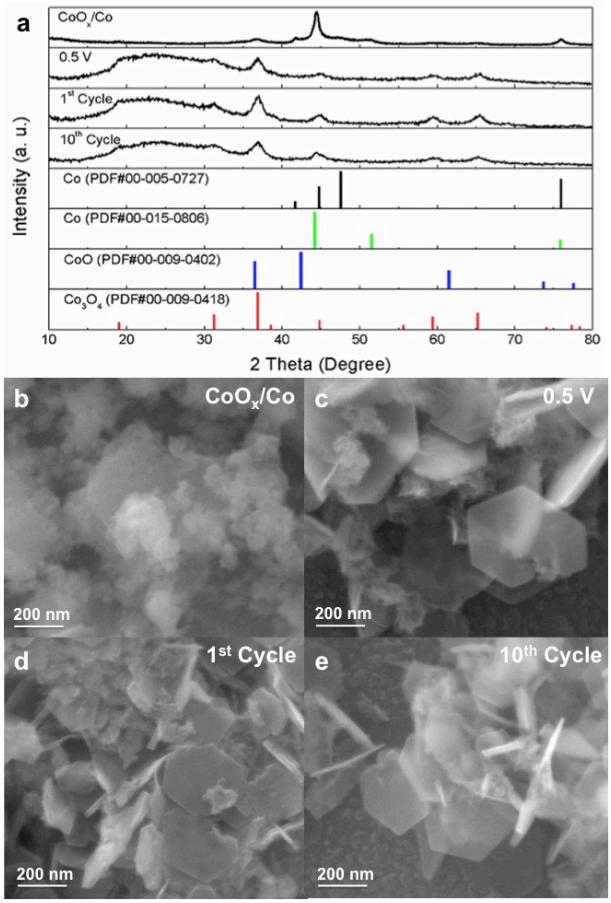

Figure 4.3: (a) X-ray diffraction (XRD) patterns of the as-prepared CoO_x/Co, electrode materials after electrochemical measurements and standard XRD patterns of possible existing cobalt or cobalt oxide phases. Scanning electron microscopy (SEM) images of (b) as-prepared CoO_x/Co, (c) electrode materials after scanning to 0.5 V *vs*. SCE, (d) electrode materials after the 1st cycle, and (e) electrode materials after the 10th cycle. The electrode materials were cast onto a 1 cm × 2 cm stainless steel sheet and scanned to 0.5 V *vs*. SCE or cycled between 0 V and 0.8 V *vs*. SCE at 30 mV s^{-1} in 1 M KOH electrolyte.

CoO_x/Co precursors were prepared through a solvothermal decomposition of $Co_4(CO)_{12}$ in hexanes in a sealed autoclave at 433 K for 24 h (see schematic pathway in Fig. 4.2a). The as-prepared black powder was then collected and characterized with X-ray diffraction (XRD) to identify the existing phases. As can be found in the XRD pattern

(see Fig. 4.3a), the as-prepared powder is a mixture of hcp-Co (PDF #00-005-0727), fcc-Co (PDF #00-015-0806), CoO (PDF #00-009-0402), and Co_3O_4 (PDF #00-009-0418), among which fcc-Co is the primary phase. The cobalt oxides (CoO and Co_3O_4) exist probably because residual air in the autoclave oxidizes a small amount of the metallic cobalt at the high temperature during the solvothermal treatment. The as-prepared CoO_x/Co precursors were then loaded on a rotating disk electrode (RDE) and cycled in 1 M KOH solution between 0 V and 0.8 V *vs*. saturated calomel electrode (SCE) with a scan rate of 30 mV s^{-1} (see the voltammograms with iR correction in Fig. 4.2b). The cyclic voltammetry (CV) results show a very broad irreversible peak from 0 V to 0.3 V *vs*. SCE in the anodic scan of the 1st cycle. This peak is attributed to the oxidation of cobalt.[34] After the 1st cycle, the subsequent cycles exhibit similar CV profiles, suggesting that the oxidation of cobalt only happens in the 1st cycle.

To better understand the oxidation process of precursors and the reaction products, CoO_x/Co ink without the addition of conductive carbon and Nafion was loaded on a 1 cm × 2 cm stainless steel sheet (see Fig. 4.1) and was scanned from 0 V to 0.5 V *vs*. SCE or cycled between 0 V and 0.8 V *vs*. SCE at 30 mV s^{-1} in 1 M KOH solution (see Fig. 4.4). The samples after electrochemical tests were then collected for further characterizations. As found in Fig. 4.4, there exists a broad irreversible peak from 0 V to 0.5 V *vs*. SCE in the 1st cycle of the sheet-loaded CoO_x/Co. The electrochemical performance difference between RDE-loaded sample and sheet-loaded sample can be attributed to the conductivity difference as a result of different ink preparation procedures. 0.5 V is chosen to be the potential point to collect sample as there is a noticeable curvature change at 0.5 V where gas bubbles start to form.

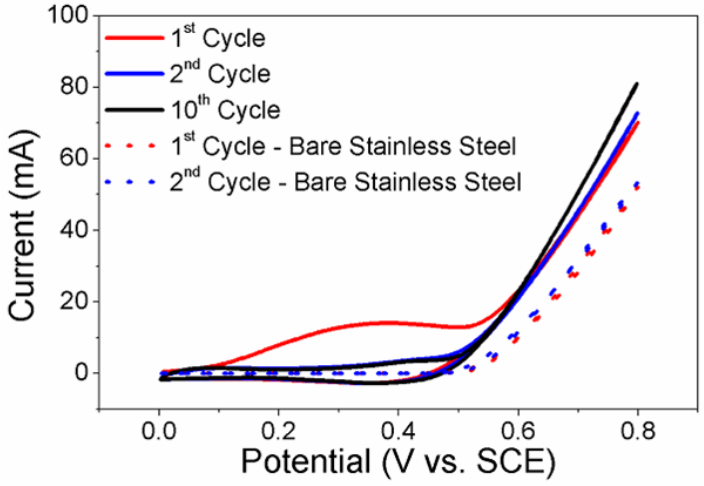

Figure: 4.4: Cyclic voltammograms of stainless steel sheet loaded with CoO_x/Co ink B (solid lines) and bare sheet (dotted lines) in 1 M KOH solution from 0 V to 0.8 V *vs*. SCE at 30 mV s^{-1}.

Samples after electrochemical tests were collected and examined with XRD to analyze the oxidation products and the associated phase transformation (see Fig. 4.3a). For samples collected after the electrochemical measurements, the broad peak from 15° to 35° is from the XRD sample holder since there was not enough material to cover the holder. As found in Fig. 4.3a, sample collected at 0.5 V *vs*. SCE in the 1st cycle exhibits characteristic XRD peaks from spinel Co_3O_4, suggesting the complete transformation of the precursors to Co_3O_4. For samples collected at the subsequent cycles, only Co_3O_4 peaks can be found, indicating that after the irreversible oxidation peak of the 1st cycle, the *in situ* electrochemical generation of Co_3O_4 is complete and Co_3O_4 serves as the catalyst for OER.

To further study whether there is morphological change associated with the oxidation of the CoO_x/Co precursor, samples on stainless steel sheets after the electrochemical tests were further observed with scanning electron microscopy (SEM).

As shown in Fig. 4.3b, the particle size of the irregular-shaped CoO_x/Co precursors ranges from 50 nm to 200 nm. However, after scanning to 0.5 V *vs*. SCE in 1 M KOH solution, CoO_x/Co precursors begin to form hexagonal nanoplate morphology with a thickness of 15 ~ 30 nm. These nanoplates are pure phase Co_3O_4 based on XRD results (Figure Fig. 4.3a). The hexagonal 2D-Co_3O_4 retains its morphology in the subsequent cycles, suggesting that the hexagonal morphology is stable within the potential range (0 V to 0.8 V *vs*. SCE) and can survive the rigorous OER.

The mechanism of morphology change can be explained by comparing with hydrothermal-prepared $Co(OH)_2$ hexagonal nanosheets.[52] First, in the potential region of the broad irreversible peak, the precursor is oxidized to $Co(OH)_2$ possessing a hexagonal morphology:

$$Co + 2OH^- \rightarrow Co(OH)_2 + 2e^-$$

Subsequently, $Co(OH)_2$ is oxidized to Co_3O_4 at higher potential while maintaining the hexagonal morphology. As previous research has suggested that $Co(IV)O_m(OH)_n$ is the active intermediate for OER, this hypothesis can explain the morphology change.[34]

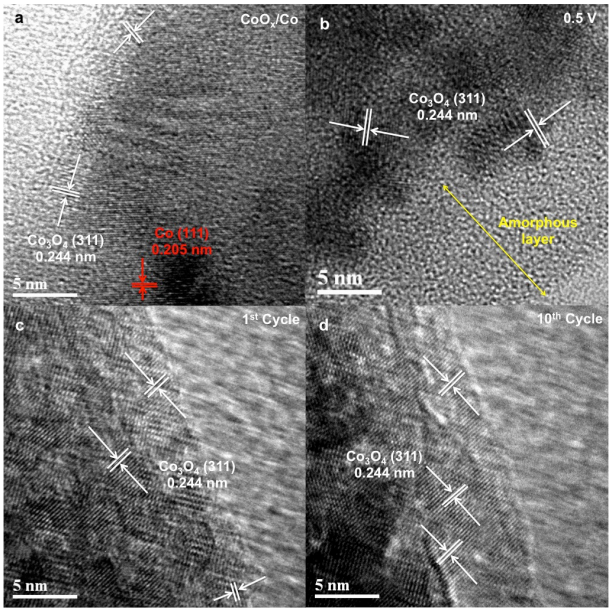

Figure 4.5: High-resolution transmission electron microscopy (HRTEM) images of (a) as-prepared CoO_x/Co, (b) electrode materials after scanning to 0.5 V *vs*. SCE, (c) electrode materials after the 1st cycle, and (d) electrode materials after the 10th cycle. The electrode materials were cast onto a 1 cm × 2 cm stainless steel sheet and scanned to 0.5 V *vs*. SCE or cycled between 0 V and 0.8 V *vs*. SCE at 30 mV s^{-1} in 1 M KOH electrolyte.

The microstructure change during the electrochemical tests was studied by high-resolution transmission electron microscopy (HRTEM, see Fig. 4.5). For the as-prepared CoO_x/Co, the bulk part of the crystal is fcc-Co. Some small Co_3O_4 crystals are attached to the surface of the fcc-Co crystals. This corresponds well with the XRD results that weak diffraction peaks from cobalt oxides co-exist with very strong fcc-Co peaks. After scanning to 0.5 V *vs*. SCE, the surface layer (about 20 ~ 40 nm) of the crystal is transformed into an amorphous phase with small Co_3O_4 crystals found inside the particle. No noticeable metallic cobalt crystals can be found from the HRTEM images. Together with the XRD results, it is reasonable to conclude that the precursor is oxidized to Co_3O_4 before the onset of OER and thus, *in situ* electrochemical preparation of 2D-Co_3O_4 is

achieved. Interestingly, after scanning the electrodes back to 0 V *vs*. SCE, crystalized Co_3O_4 forms and the amorphous layer disappears. This indicates that the catalysts undergo certain phase transformation during the back scan in KOH electrolyte. As the Co(II)/Co(III) redox couple in Co_3O_4 go through a transition to Co(III)/Co(IV) upon charging, the formation and the disappearance of the amorphous layer could be the result of the dissolution/redeposition mechanism of the Co(II), similar to that found in $LiCoPO_4$.[8]

4.3.2 Electrochemical Performance Evaluation

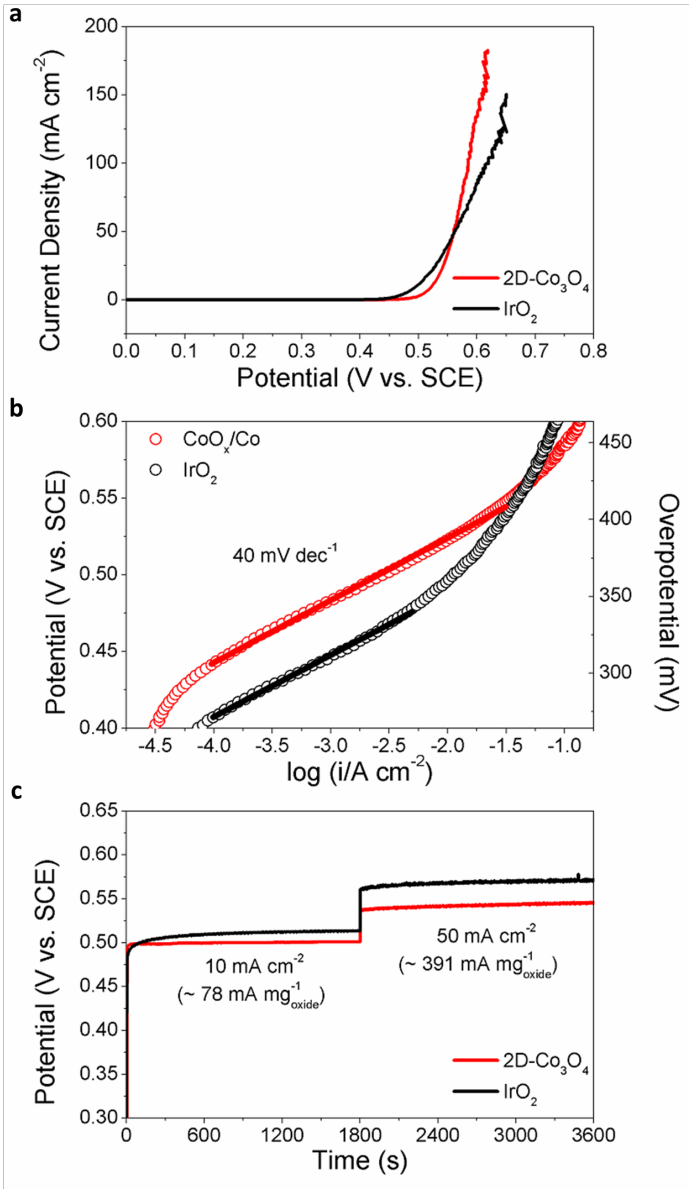

Figure 4.6: (a) Rotating disk electrode voltammograms of 2D-$Co_3O_4$and IrO_2 after iR correction at a scan rate of 1 mV s^{-1}. (b) Tafel plots of catalysts cast onto a glassy carbon rotating disk electrode recorded at 1 mV s^{-1} in 1 M KOH. (c) Chronopotentiometry curves of 2D-$Co_3O_4$and IrO_2 catalysts on rotating disk electrode after iR correction at constant current densities of 10 and 50 mA cm^{-2}. All electrochemical experiments were conducted in 1 M KOH electrolyte with the rotation speed of 2000 rpm.

To study the catalytic activity and stability of the 2D-Co_3O_4, the as-prepared CoO_x/Co precursor was loaded on a rotating disk electrode (RDE) for further electrochemical tests. The RDEs were first cycled between 0 V and 0.8 V *vs*. SCE for three cycles to prepare 2D-Co_3O_4 and then tested with linear sweep voltammetry (LSV) or chronopotentiometry. The electrochemical property of commercial IrO_2 (Alfa Aesar) was also examined as a benchmark. As shown in Fig. 4.6a, while IrO_2 exhibits a lower onset potential, 2D-Co_3O_4 shows larger current densities at higher potentials (> 0.55 V *vs*. SCE). The potential at 10 mA cm^{-2} is 0.52 V *vs*. SCE for 2D-Co_3O_4, compared to 0.50 V *vs*. SCE for IrO_2. At 100 mA cm^{-2}, the potential for 2D-Co_3O_4 is 0.58 V *vs*. SCE while it is 0.62 V *vs*. SCE for IrO_2.

To understand the high catalytic activity of 2D-Co_3O_4, Tafel slopes beyond the onset potential of 2D-Co_3O_4 and IrO_2 were calculated and shown in Fig. 4.6b. The Tafel slopes for both 2D-Co_3O_4 and IrO_2 are about 40 mV dec^{-1} at relative low overpotential and increase quickly at higher overpotential. The increase of the Tafel slope indicates a decrease of charge-transfer kinetics of the catalytic reaction. This could be the result of reaction mechanism change or reduced reaction area due to the formation of the oxygen bubbles on the surface of electrodes, which cannot be neglected at relatively high current densities.[34, 35] As shown in Fig. 4.6b, the potential window with Tafel slope of ~ 40 mV dec^{-1} is wider for 2D-Co_3O_4 (~ 0.44 V to 0.55 V *vs*. SCE) compared to IrO_2 (~ 0.41 V to 0.47 V *vs*. SCE). This is probably due to the special 2D nanoplate structure of the 2D-Co_3O_4, which can effectively release the oxygen bubbles and provide more active sites for OER.[29, 36] The chronopotentiometry tests also suggest that 2D-Co_3O_4 exhibits better catalytic activity and stability compared to IrO_2, especially at higher current densities (see Fig. 4.6c), which is very desirable for applications in metal-air batteries.

4.4 CONCLUSION

The hexagonal 2D-Co_3O_4 nanoplates with thickness of 15 ~ 30 nm are prepared through an *in situ* electrochemical method. Electron microscopy along with XRD characterizations suggest that the CoO_x/Co precursors are oxidized to Co_3O_4 within the broad irreversible peak before the onset potential of OER in the first cycle of the CV tests. Associated with the oxidation process, the morphology of the catalysts undergoes a transformation from irregular-shaped CoO_x/Co precursors to 2D hexagonal Co_3O_4 nanoplates. Amorphization and recrystallization of the catalysts are also found during the electrochemical tests. The 2D-Co_3O_4 exhibits excellent OER catalytic activity and stability probably due to the 2D structure, which can effectively release oxygen bubbles and provide more active sites for catalytic reactions. These findings can provide a fast *in situ* electrochemical method to prepare highly active 2D cobalt oxides for water electrolysis and metal-air batteries.

Chapter 5: Summary

This thesis focused on the synthesis and a systematic study of Co_3O_4-based catalysts for ORR and OER. As promising low-cost candidates to replace the expensive Pt/C and IrO_2 to catalyze ORR and OER in alkaline solutions, Co_3O_4-based catalysts have attracted great research interest. The goal of this thesis was to delineate the respective roles of Co_3O_4 and carbon materials in catalyzing ORR and OER and to design novel synthesis methods to prepare nano-sized Co_3O_4 materials. The findings in this thesis will be of great value for catalysis and metal-air battery fields.

It was found that Co_3O_4 alone exhibited poor ORR catalytic activity, but assisted the selective four-electron oxygen reduction over the two-electron pathway in the presence of CNW. Co_3O_4 acted as the primary catalytic site for OER and enhanced the stability of CNW in the OER potential region. CNW improved the electronic conduction between Co_3O_4 and the current collector. The enhancement in the catalytic stability in the OER potential region is mainly due to the preference of OER over the degradation of CNW as a result of the improved OER kinetics.

An *in situ* electrochemical generation of 2-dimensional Co_3O_4 hexagonal nanoplates was achieved and the OER catalytic performance of the 2D-Co_3O_4 was evaluated. Electron microscopy and XRD results showed that the transformation from CoO_x/Co to 2D-Co_3O_4 was accompanied by morphological and crystal structural changes before the onset potential of OER. The 2D-Co_3O_4 exhibited excellent OER catalytic activity and stability due to the effective mass transfer through the 2D structure.

The outcomes of this thesis are that it has provided more insights into the individual functionalities of Co_3O_4 and carbon materials beyond the synergistic effects and provided novel pathway to prepare nano-sized Co_3O_4. More efforts should be devoted

to understand the degradation mechanism of carbon materials in the OER potential region and scale up production of proper Co_3O_4-based catalysts to achieve the industrialization of metal-air battery technology.

Appendix: List of Publications

1. Liu, S.; Li, L.; Ahn, H. S.; Manthiram, A. *J. Mater. Chem. A.* **2015***, 3,* 11615 – 11623.
2. Liu, S; Li, L.; Patterson, N. A.; Manthiram A. Submitted to *ACS Applied Materials & Interfaces.*
3. Li, L.; Liu, S.; Manthiram, A. *Nano Energy* **2015**, *12*, 852–860.

References

1. Bruce, P. G.; Freunberger, S. A.; Hardwick, L. J.; Tarascon, J.-M. *Nature Materials* **2011**, *11*, 19–29.
2. Cheng, F.; Chen, *J. Chem. Soc. Rev.* **2012**, *41*, 2172–2192.
3. Girishkumar, G.; McCloskey, B.; Luntz, A. C.; Swanson, S.; Wilcke, W. *J. Phys. Chem. Lett.* **2010**, *1*, 2193–2203.
4. Steele, B. C.; Heinzel, A. *Nature* **2001**, *414*, 345–352.
5. Li, L.; Zhao, X.; Manthiram, A. *Electrochemistry Communications* **2012**, *14*, 78–81.
6. Park, M.; Sun, H.; Lee, H.; Lee, J.; Cho, J. *Adv. Energy Mater.* **2012**, *2*, 780–800.
7. Black, R.; Adams, B.; Nazar, L. F. *Adv. Energy Mater.* **2012**, *2*, 801–815.
8. Lee, S. W.; Carlton, C.; Risch, M.; Surendranath, Y.; Chen, S.; Furutsuki, S.; Yamada, A.; Nocera, D. G.; Shao-Horn, Y. *J. Am. Chem. Soc.* **2012**, *134*, 16959–16962.
9. Li, L.; Manthiram, A. *J. Mater. Chem. A* **2013**, *1*, 5121–5127.
10. Yoo, E.; Zhou, H. *ACS Nano* **2011**, *5*, 3020–3026.
11. Liang, Y.; Wang, H.; Zhou, J.; Li, Y.; Wang, J.; Regier, T.; Dai, H. *J. Am. Chem. Soc.* **2012**, *134*, 3517–3523.
12. Liang, Y.; Li, Y.; Wang, H.; Zhou, J.; Wang, J.; Regier, T.; Dai, H. *Nature Materials* **2011**, *10*, 780–786.
13. Cheng, F.; Shen, J.; Peng, B.; Pan, Y.; Tao, Z.; Chen, J. *Nature Chem* **2010**, *3*, 79–84.

14. Lee, J.-S.; Tai Kim, S.; Cao, R.; Choi, N.-S.; Liu, M.; Lee, K. T.; Cho, J. *Adv. Energy Mater.* **2010**, *1*, 34–50.

15. Gong, K.; Du, F.; Xia, Z.; Durstock, M.; Dai, L. *Science* **2009**, *323*, 760-764.

16. Wang, S.; Yu, D.; Dai, L. *J. Am. Chem. Soc.* **2011**, 133, 5182–5185.

17. Qu, L.; Liu, Y.; Baek, J.-B.; Dai, L. *ACS Nano* **2010**, *4*, 1321–1326.

18. Wiggins-Camacho, J. D.; Stevenson, K. J. *J. Phys. Chem. C* **2011**, *115*, 20002–20010.

19. Maldonado, S.; Stevenson, K. J. *J. Phys. Chem. B* **2005**, *109*, 4707–4716.

20. Liu, R.; Wu, D.; Feng, X.; Müllen, K. *Angew. Chem. Int. Ed.* **2010**, *49*, 2565–2569.

21. Liang, H. W.; Zhuang, X.; Brüller, S.; Feng, X.; Müllen, K. *Nature Communications* **1AD**, *5*, 1–7, DOI:10.1038/ncomms5973.

22. Li, L.; Manthiram, A. *Adv. Energy Mater.* **2014**, *4*, 1-7, DOI: 10.1002/aenm.201301795

23. Suntivich, J.; May, K. J.; Gasteiger, H. A.; Goodenough, J. B.; Shao-Horn, Y. *Science* **2011**, *334*, 1383–1385.

24. Bockris, J. O.; Otagawa, T. *J. Phys. Chem.* **1983**, *87*, 2960–2971.

25. Shimizu, Y.; Uemura, K.; Matsuda, H.; Miura, N.; Yamazoe, N. *J. Electrochem. Soc.* **1990**, *137*, 3430–3433.

26. Sunarso, J.; Torriero, A. A. J.; Zhou, W.; Howlett, P. C.; Forsyth, M. *J. Phys. Chem. C* **2012**, *116*, 5827–5834.

27. May, K. J.; Carlton, C. E.; Stoerzinger, K. A.; Risch, M.; Suntivich, J.; Lee, Y.-L.; Grimaud, A.; Shao-Horn, Y. *J. Phys. Chem. Lett.* **2012**, *3*, 3264–3270.

28. Li, Y.; Gong, M.; Liang, Y.; Feng, J.; Kim, J.-E.; Wang, H.; Hong, G.; Zhang, B.; Dai, H. *Nature Communications* **1AD**, *4*, 1805–1807, DOI:10.1038/ncomms2812.

29. Gong, M.; Li, Y.; Wang, H.; Liang, Y.; Wu, J. Z.; Zhou, J.; Wang, J.; Regier, T.; Wei, F.; Dai, H. *J. Am. Chem. Soc.* **2013**, *135*, 8452–8455.

30. Gong, M.; Li, Y.; Zhang, H.; Zhang, B.; Zhou, W.; Feng, J.; Wang, H.; Liang, Y.; Fan, Z.; Liu, J.; Dai, H. *Energy Environ. Sci.* **2014**, *7*, 2025–2032.

31. Louie, M. W.; Bell, A. T. J. *Am. Chem. Soc.* **2013**, *135*, 12329–12337.

32. Lyons, M. E. G.; Brandon, M. P. *Int. J. Electrochem. Sci.* **2008**, *3*, 1386–1424.

33. Lyons, M. E. G.; Brandon, M. P. *Journal of Electroanalytical Chemistry* **2010**, *641*, 119–130.

34. Lyons, M. E. G.; Brandon, M. P. *Int. J. Electrochem. Sci.* **2008**, *3*, 1425–1462.

35. Hamdani, M.; Singh, R. N.; Chartier, P. *Int. J. Electrochem. Sci.* **2010**, *5*, 556–577.

36. Li, L.; Chai, S.-H.; Dai, S.; Manthiram, A. *Energy Environ. Sci.* **2014**, *7*, 2630–2636.

37. Maiyalagan, T.; Jarvis, K. A.; Therese, S.; Ferreira, P. J.; Manthiram, A. *Nature Communications* **1AD**, *5*, 1–8, DOI:10.1038/ncomms4949.

38. Liu, Y.; Higgins, D. C.; Wu, J.; Fowler, M.; Chen, Z. *Electrochemistry Communications* **2013**, *34*, 125–129.

39. Bian, W.; Yang, Z.; Strasser, P.; Yang, R. *Journal of Power Sources* **2014**, *250*, 196–203.

40. Zhai, X.; Yang, W.; Li, M.; Lv, G.; Liu, J.; Zhang, X. *Carbon* **2013**, *65*, 277–286.

41. Chen, S.; Qiao, S.-Z. *ACS Nano* **2013**, *7*, 10190–10196.

42. Peng, C.; Chen, B.; Qin, Y.; Yang, S.; Li, C.; Zuo, Y.; Liu, S.; Yang, J. *ACS Nano* **2012**, *6*, 1074–1081.

43. Ha, D.-H.; Moreau, L. M.; Honrao, S.; Hennig, R. G.; Robinson, R. D. *J. Phys. Chem. C* **2013**, *117*, 14303–14312.

44. Du, N.; Zhang, H.; Chen, B. D.; Wu, J. B.; Ma, X. Y.; Liu, Z. H.; Zhang, Y. Q.; Yang, D. R.; Huang, X. H.; Tu, J. P. *Adv. Mater.* **2007**, *19*, 4505–4509.

45. Su, F.; Lv, L.; Lee, F. Y.; Liu, T.; Cooper, A. I.; Zhao, X. S. *J. Am. Chem. Soc.* **2007**, *129*, 14213–14223.

46. Zhang, L. L.; Wei, T.; Wang, W.; Zhao, X. S. *Microporous and Mesoporous Materials* **2009**, *123*, 260–267.

47. Wu, Z.-S.; Yang, S.; Sun, Y.; Parvez, K.; Feng, X.; Müllen, K. *J. Am. Chem. Soc.* **2012**, *134*, 9082–9085.

48. Ma, C. Y.; Mu, Z.; Li, J. J.; Jin, Y. G.; Cheng, J.; Lu, G. Q.; Hao, Z. P.; Qiao, S.-Z. *J. Am. Chem. Soc.* **2010**, *132*, 2608–2613.

49. Kong, F. *Electrochimica Acta* **2012**, *68*, 198–201.

50. Deng, X.; Schmidt, W. N.; Tüysüz, H. *Chem. Mater.* **2014**, *26*, 6127–6134.

51. He, T.; Chen, D.; Jiao, X.; Wang, Y. *Adv. Mater.* **2006**, *18*, 1078–1082.

52. Zhan, F.; Geng, B.; Guo, Y. *Chem. Eur. J.* **2009**, *15*, 6169–6174.